Widespread neural and autonomic system synchrony across the brain-body axis

Taylor Bolt[1], Shiyu Wang[2], Jason S. Nomi[1], Roni Setton[5], Benjamin P. Gold[3], Blaise deB.Frederick[6], B.T. Thomas Yeo[7], J Jean Chen[8,9,10] , Dante Picchioni[11], R Nathan Spreng[12], Shella D. Keilholz[13], Lucina Q. Uddin[1]*, Catie Chang[2,3,4]*

[1] Department of Psychiatry and Biobehavioral Sciences, University of California, Los Angeles, Los Angeles, CA, USA

[2] Department of Biomedical Engineering, Vanderbilt University, Nashville, TN, USA

[3] Departments of Electrical and Computer Engineering, Vanderbilt University, Nashville, TN, USA

[4] Department of Computer Science, Vanderbilt University, Nashville, TN, USA

[5] Department of Psychology, Harvard University, Boston, MA, USA

[6] Brain Imaging Center McLean Hospital, Harvard Medical School, Belmont, Massachusetts

[7] Department of Electrical & Computer Engineering, Centre for Translational MR Research, Centre for Sleep & Cognition, N.1 Institute for Health and Institute for Digital Medicine, National University of Singapore, Singapore

[8] Rotman Research Institute, Baycrest Health Sciences, Toronto, Canada.

[9] Department of Medical Biophysics, University of Toronto, Toronto, Canada.

[10] Institute of Biomedical Engineering, University of Toronto, Toronto, Canada.

[11] Advanced MRI Section, Laboratory of Functional and Molecular Imaging, National Institute of Neurological Disorders and Stroke, National Institutes of Health; Bethesda, MD, United States

[12] Montreal Neurological Institute, Department of Neurology and Neurosurgery, McGill University, Montreal, QC, Canada

[13] Emory University/Georgia Institute of Technology, Atlanta, GA, USA

*Contributed equally

Abstract

The brain is closely attuned to visceral signals from the body's internal environment, as evidenced by the numerous associations between neural and peripheral physiological signals. This study describes a synchrony in the low-frequency range (0.01 - 0.1 Hz) between global brain hemodynamics, neural activity, and a host of autonomic signals spanning cardiovascular, pulmonary, exocrine and smooth muscle systems. We show that this brain-body synchrony can

be captured by a single spatiotemporal pattern across fMRI, EEG and peripheral physiological signals in human subjects. These findings are replicated across several independent samples and data acquisition systems. Furthermore, this spatiotemporal pattern of brain-body synchrony is elicited by autonomic arousal in deep breathing, spontaneous K-complexes during sleep, and the delivery of intermittent sensory stimuli, as well as at rest. Further, we show that the spatial structure of global brain hemodynamics is maintained under experimental suppression of end-tidal carbon dioxide (PETCO2) variations, suggesting that respiratory-driven fluctuations in arterial CO2 accompanying arousal cannot explain the origin of these hemodynamic signals in the brain. These findings suggest that the origin of low-frequency global brain hemodynamics may be mediated by ascending arousal system projections, which modulate widespread neuronal activity as well as sympathetic vasoconstrictive effects on the cerebral vasculature. The prominence of this brain-body synchrony during deep breathing provides a mechanistic understanding of the positive health benefits of diaphragmatic breathing and may inform psychological therapeutic techniques for anxiety and stress.

Introduction

The communication of visceral signals from the body's internal environment to the brain is essential for adaptive behavior. Central autonomic nuclei are closely connected to ascending arousal system nuclei that project diffusely to the cortex and subcortex, influencing wakefulness, affect and interoception (Satpute et al., 2019; Yackle et al., 2017). Pharmacological and electrical stimulation of central autonomic nuclei (e.g. solitary nucleus) produces widespread cortical EEG synchronization, suggesting a role for these structures in arousal and wakefulness fluctuations (Anaclet & Fuller, 2017; Dringenberg & Vanderwolf, 1998). It remains unclear whether central autonomic nuclei are causally responsible for widespread fluctuations of cerebral blood flow and oxygenation in the brain that represent the dominant source of variance in spontaneous low-frequency (~0.01-0.1Hz) fluctuations in blood-oxygen level dependent (BOLD) signals (Fox & Raichle, 2007; Liu et al., 2017). Global hemodynamic fluctuations measured by functional magnetic resonance imaging (fMRI) have been associated with peripheral physiological signals from effector organs of the autonomic nervous system (ANS) (e.g. heart rate, respiratory volume, pupil diameter) (Birn et al., 2008; Chang et al., 2009; Özbay et al., 2019; Power et al., 2017; Shams et al., 2021; Yellin et al., 2015). Covariation with multiple autonomic signals suggests that global brain fluctuations measured with fMRI/EEG may form one component of a larger, integrated physiological network spanning multiple organ systems governed by the ANS. Previous studies provide support for this hypothesis, showing that global hemodynamic and EEG power fluctuations covary closely in time with peripheral physiological recordings from the respiratory system, cardiovascular and peripheral vasculature (Gu et al., 2022), and may reflect spontaneous fluctuations in arousal (Raut et al., 2021, 2023).

This study seeks to demonstrate the degree of coordination between low-frequency (0.01 - 0.1Hz) global brain fluctuations measured with fMRI/EEG and autonomic signaling across multiple ANS effector organs. Using multiple independent samples of multi-modal fMRI,

EEG and peripheral physiological recordings acquired during resting state, we demonstrate that a single, low-dimensional projection captures a major axis of covariation between global brain fluctuations and widespread peripheral physiological dynamics, including pulmonary (respiratory variability), cardiovascular (heart rate variability), exocrine (skin conductance) and smooth muscle (peripheral vascular tone & pupil diameter) systems. The timing of the temporal dynamics within and between modalities suggest that the ANS may have a direct role in the origin of spontaneous global brain fluctuations. Spontaneous variations in autonomic arousal (K-complexes) during sleep, as well as direct manipulation of autonomic activity via deep breathing and sensory stimulation, induced a similar pattern of co-fluctuations between the brain and body. Experimental suppression of spontaneous variations in end-tidal carbon dioxide (PETCO2) accompanying arousal demonstrated that arterial CO2 cannot explain the origin of these global brain fluctuations. Taken together, these findings provide novel evidence for the role of the autonomic system in governing spontaneous global fluctuations commonly observed in fMRI and EEG data.

Results

Global Hemodynamic Fluctuations Are Embedded in a Low-Frequency Physiological Network

Global hemodynamic fluctuations were extracted via the first principal component (PC1) of whole-brain BOLD fMRI time courses. In a previous report (Bolt et al., 2022), the first PC was found to account for a variety of previously observed empirical phenomena in spontaneous BOLD activity, including much of the global spatial structure of whole-brain functional connectivity. Examination of the spatiotemporal structure of spontaneous global BOLD signals across cortical and subcortical structures via complex PCA (Bolt et al., 2022) (**Figure 1A; Supplementary Movie 1; Supplementary Figure 1**) reveals a characteristic sequence across datasets: large amplitude BOLD increases in gray and white matter, followed by a propagation of BOLD signals towards the location of large draining veins and CSF compartments. The spatial distribution of the first principal component for each dataset is displayed in **Supplementary Figure 2**.

Analysis of six separate resting-state fMRI datasets (ME-REST, ME-REST-SUPP, HCP-REST, NATVIEW-REST, NKI-REST, and YALE-REST) shows that global BOLD fluctuations covary with a multitude of peripheral physiological signals (**Figure 1B**), including respiratory volume, heart rate, peripheral vascular tone (measured via the low-frequency component - 0.01-0.1 Hz, and the pulse amplitude of the pulse oximeter signal), skin conductance, and pupil diameter. Analysis of the relationship between surface EEG power fluctuations and global BOLD signal in two simultaneous EEG-fMRI datasets (ME-REST, NATVIEW-REST) reveals co-synchrony between global BOLD signals and neuronal oscillations across a wide band of frequencies (2 - 20Hz). Most cross-correlation plots exhibit two distinct peaks for all signals, indicating synchrony between physiological signals and the global BOLD signal at two distinct time lags: 1) a negative or zero time lag (0 to ~5 secs) of the global BOLD

signal, indicating that the physiological signal follows, or is simultaneous with the global BOLD signal, respectively, and 2) a positive lag (0 to ~10s) of the global BOLD signal, indicating that the physiological signal precedes the global BOLD signal. To summarize the temporal lags between all recorded physiological signals, we estimated impulse response functions (see *Methods and Materials*) (Chang et al., 2009) of each physiological signal to an impulse of the global BOLD signal from three separate datasets: ME-REST (PPG signals, Alpha EEG power, and respiratory volume), NATVIEW-REST (pupil), and NKI-REST datasets (skin conductance) (**Figure 1C**).

These cross-correlations establish pairwise relationships between global BOLD signals and physiological signals, but do not provide definitive evidence of a global co-synchrony between all pairs of signals across time. To establish the latter, we performed a cross-decomposition between all pairs of signals and their lags via multi-set canonical correlation analysis (MCCA; see *Methods and Materials*). Our aim was to examine whether the joint co-fluctuations between all signals (and their time-lags) can be extracted in a single latent dimension. Note, though the relationship between global BOLD and EEG power is broadband (see **panel B**), we included alpha (8-12Hz) EEG power as a single signal from the EEG due to previous reports of a relationship between alpha power and global BOLD signals (Yuan et al., 2013). Application of MCCA to five resting-state fMRI datasets demonstrates that the first canonical component (**Figure 1D**), representing the latent component with the maximal average pairwise correlation between all pairs of signals, captures moderate pairwise correlations between all signals, including peripheral physiology, neuronal (alpha EEG power) and global BOLD (PC1) signals (e.g ME-REST: $\bar{r}$ = 0.31, p = 0.001). Further, the global BOLD signal exhibits the strongest pairwise correlations among all signals within the first canonical component across datasets. Time lags between signals in the first canonical component are presented in **Supplementary Figure 9**.

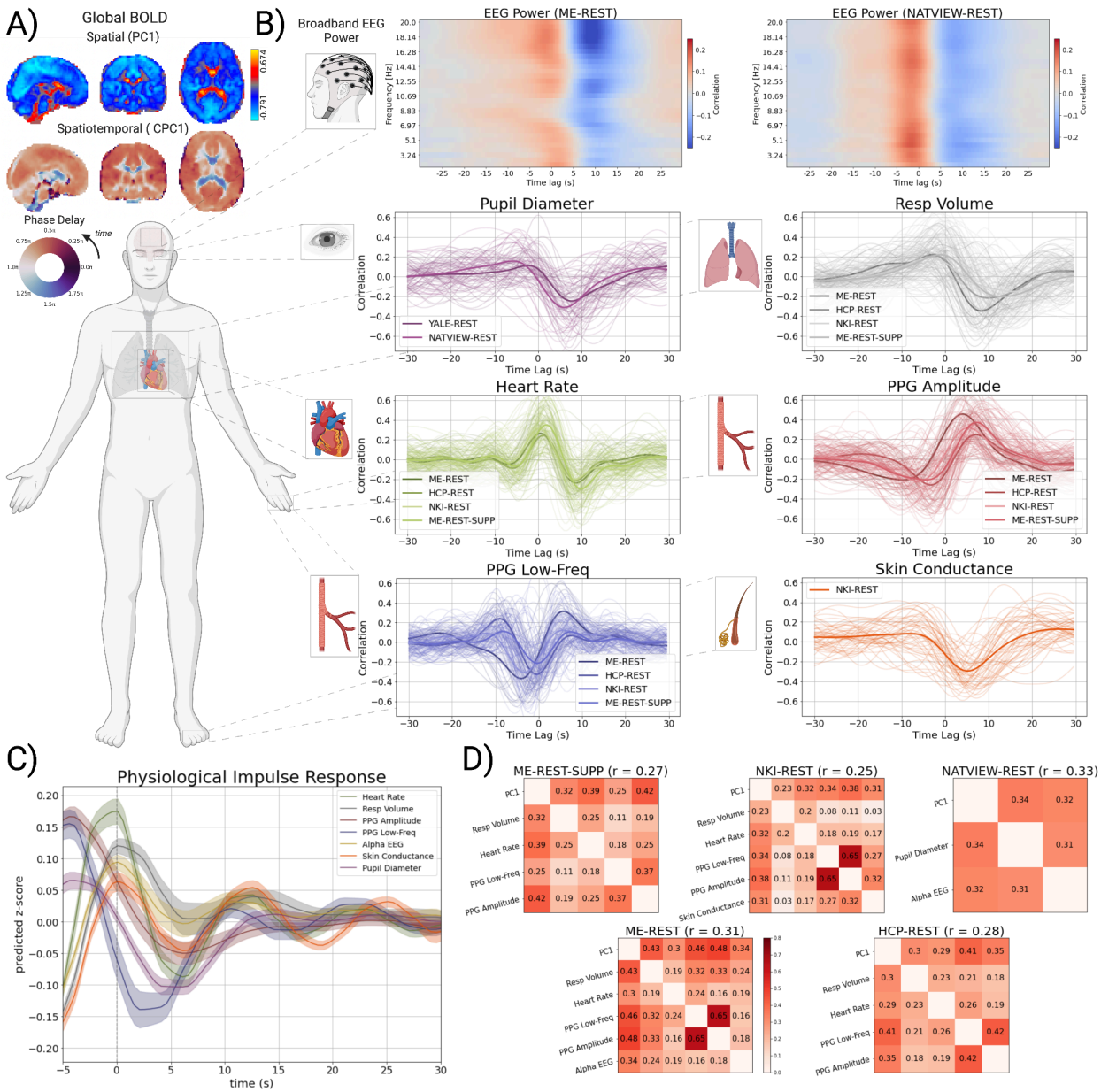

Figure 1. **Global Hemodynamic Fluctuations Are Embedded in a Low-Frequency Physiological Network.** The cross-correlation between the time courses of the global BOLD signal (first principal component; PC1) and multiple physiological signals. **A)** The spatial weights of the first principal component (PC1; top), and the phase delay map of the first complex principal component (CPC1; bottom) from the ME-REST dataset. The phase delay map of the first complex principal component encodes the time-delay (in radians) between voxels within the component. Because phase delay is measured in radians (0 to 2pi) they are displayed with a circular color map. **B)** Cross-correlation plots of each physiological signal with the global BOLD time course (PC1). The cross-correlation is defined as the correlation coefficient between x_{t+i} and y_t where *t* is the time index, *i* is $\pm$ 30 secs (i.e. the index along the x-axis of the plots), and x is the global BOLD signal and y is the physiological signal. Strong correlation at a positive time lag (i.e. positive *i* index) indicates that the global BOLD signal lags or follows the physiological signal, while strong correlation at a negative time lag (i.e. negative *i* index) indicates that the

global BOLD signal leads the physiological signal. Within a dataset, all subject-level cross-correlations are displayed in lighter, more transparent color, while the mean signal across subjects is displayed in a darker color. Each dataset is displayed in a separate shade of the same color. Cross-correlations between global BOLD signals and wavelet filtered EEG power signals (Morlet wavelet; number of cycles = 15) for the ME-REST and NATVIEW-REST datasets are displayed as a heat map in the top panel. **C)** Estimated impulse response functions for each physiological signal in response to an impulse of the global BOLD signal. **D)** The pairwise correlations between all physiological signals (including the global BOLD signal; PC1) in the first canonical component of the MCCA analysis. The average pairwise correlation is displayed beside the title of each correlation matrix. The pairwise correlations of the first canonical component indicate a strong, joint co-fluctuation between all physiological signals and the global BOLD signal across all datasets.

Autonomic Stimuli Elicit Co-Fluctuations of the Brain-Body Physiological Network

If the ANS is the source of this global synchrony across brain and body, arousal-related stimuli should produce a similar pattern of global synchrony as that observed at rest (**Figure 1**). To provide empirical support for this hypothesis, we performed event-related averaging on fMRI, EEG and physiological signals from 1) a cued deep inhalation task (ME-TASK), 2) a cued reaction time task (ME-TASK-CUE), and 3) K-complex onsets for participants who fell asleep during the resting-state session of the ME-REST dataset. The cued deep inhalation task (ME-TASK) was a sparse event-related design with individual cues separated by one to two minutes, allowing for an estimation of the physiological impulse response to isolated inhalations without overlapping responses. The cued reaction time task was a sparse event-related design similar to the deep inhalation task, but a button response was performed in response to the cue. Consistent with a previous study (Özbay et al., 2019), we also chose to examine physiological responses in and around K-complex onsets during stage II sleep, which was found in a subset of participants of the ME-REST dataset. The K-complex is a characteristic high-amplitude EEG event that occurs predominantly in stage II sleep, and reflects phasic arousal events from internal (interoceptive) or external stimuli (Cash et al., 2009; Halász et al., 2004). K-complex annotations were performed in a semi-automated fashion on the EEG time courses of the ME-REST dataset (see *Methods and Materials*) and manually reviewed for accuracy.

Global BOLD signals (PC1) exhibit large amplitude fluctuations to isolated deep inhalations (ME-TASK) (**Figure 2A**). Consistent with the shape of the respiration response function described by Birn et al. (2008), global BOLD signals exhibit a bimodal response to inhalation, with an early positive increase (~4s) followed by a prolonged undershoot reaching its trough around ~14s. In response to isolated deep inhalations, physiological signals exhibit temporal dynamics consistent with increased ANS activity (**Figure 2A**), and lead-lag timing that is similar to that observed at rest (**Figure 1**). An increase in heart rate, broadband EEG power (**Figure 2B**), and peripheral vasoconstriction is observed around the same time as the early positive peak (~4s) of the global BOLD signal. Shortly after the global BOLD peak, a decline in heart rate is observed around the time of exhalation (~6s). Later peaks of physiological signals occur around the time of the undershoot of the global BOLD signal (~14s), including peripheral vasodilation and a rebound in heart rate.

The physiological response to a paced inhalation/breath hold task was also examined (NKI-TASK). As opposed to the sparse-event design of the inhalation task, this task was organized in sequential blocks with deep inhalations/exhalations followed by a prolonged breath hold (18s). This task structure was found to also elicit strong amplitude fluctuations in peripheral physiology and global BOLD signals with peak/trough timings largely consistent with the deep inhalation task (**Supplementary Figure 3**).

To demonstrate this spatiotemporal pattern of physiological dynamics is not specific to breathing, but to arousal-inducing stimuli more broadly, we examined physiological dynamics during a simple reaction time task, where button presses were performed in response to intermittent auditory cues. While smaller in magnitude, a similar spatiotemporal pattern was observed in button responses (**Figure 2A**), though the undershoot of the global BOLD signal occurred several seconds earlier in the button response compared to the deep inhalations. To further probe whether this brain-body physiological response may arise from stimulus-induced autonomic responses, we used the pulse wave amplitude measured from a photoplethysmograph (PPG) signal to select those trials where a peripheral vascular response at the fingertip was observed (i.e. a PPG amplitude < -1 z-score within the first ten seconds of the trial). Forty-five percent of button response trials met the criteria for a peripheral vascular response, and averaging over these trials revealed a similar but strongly amplified version of the same spatiotemporal pattern across the full set of brain and physiological signals compared to the average across all events (**Figure 2C**).

We also examined whether spontaneous autonomic arousals produced similar physiological responses as that observed in resting-state, external stimuli, and deep breathing. Event-related averages of physiological and global BOLD signals around K-complex onsets revealed the same pattern of physiological response as that observed in deep breathing, as well as that observed spontaneously during rest (**Figure 2A-**).

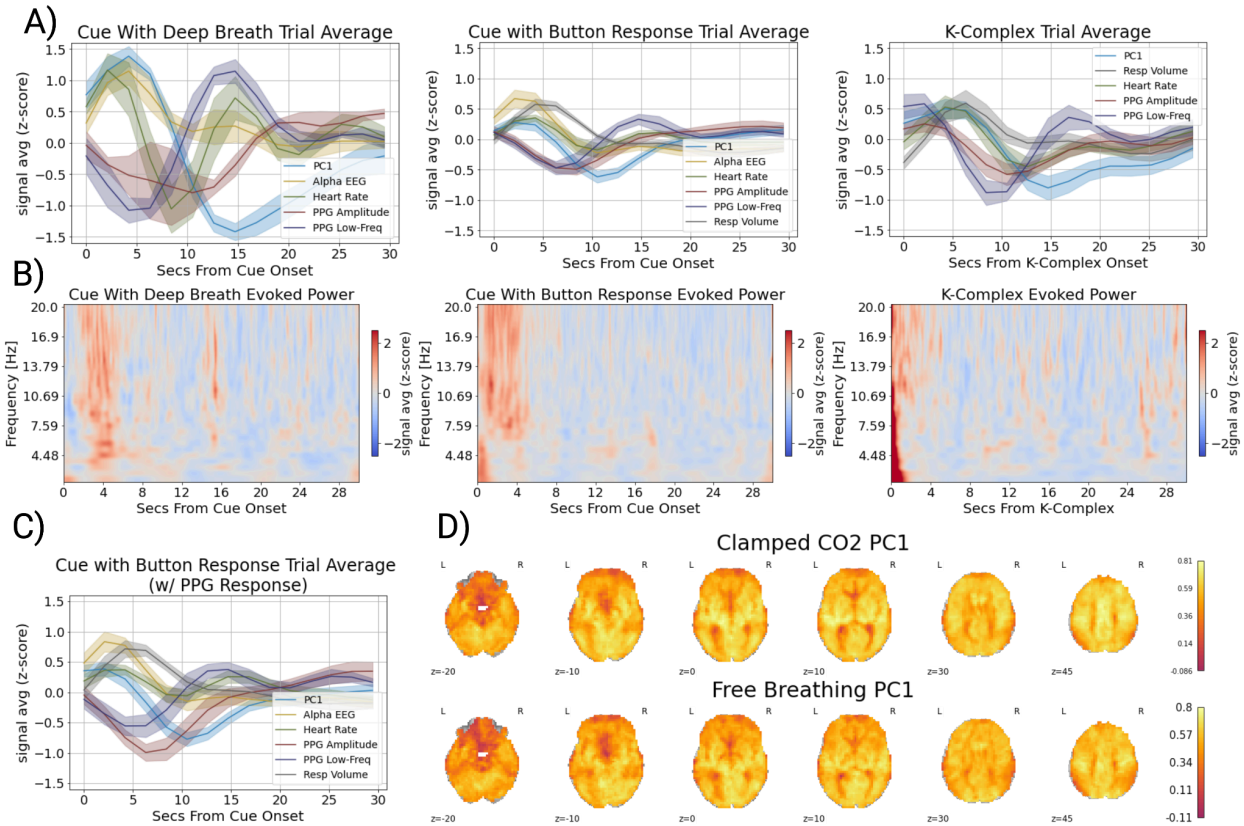

Figure 2. **Arousal Changes Generate Joint BOLD-Physiological Co-Fluctuations. A)** Event-related averages of physiological signals and global BOLD signals in response to inhalation with an auditory cue (left), an auditory cue with button response (middle) and K-complexes during sleep (right). Averages are displayed in z-score units. Standard error bars for the physiological time courses are constructed via cluster bootstrapping (i.e. resampling at the subject level; number of samples = 100). The strongest amplitude responses were observed in inhalation trials. A similar pattern of responses were observed in response to auditory cues with button responses and around spontaneous K-complexes during sleep, but with smaller magnitude. **B)** Evoked EEG power averages to inhalation with an auditory cue (left), an auditory cue with button response (middle) and K-complexes during sleep (right) were constructed through trial-averaging of Morlet wavelet filtered power signals within subjects (see Methods), followed by group-averaging across subject-trial averages. **C)** Event-related average of physiological signals and global BOLD in response to an auditory cue with a button response where a vascular response (PPG amplitude < -1 z score) was present. **D**) The spatial weights of the first principal component (PC1; global BOLD signal) estimated from a free breathing and 'clamped' CO2 condition.

Global BOLD Signals Under Clamped CO2 Conditions

One potential source of global BOLD fluctuations in response to arousal related stimuli is changes in cerebral blood flow due to levels of arterial CO2, a vasodilator (Battisti-Charbonney et al., 2011; Wise et al., 2004). As has been shown in the current study and others (e.g., Gu et al., 2022), changes in respiratory volume (respiratory rate and depth) can induce, as well as

accompany, arousal state changes. Sustained changes in respiratory volume modulate the level of arterial CO2, thereby potentially increasing cerebral blood flow (Birn et al., 2006; Wise et al., 2004). We sought to eliminate spontaneous fluctuations in arterial CO2 as the sole explanation for the global BOLD fluctuations observed in this study. To do so, we examined the existence and spatial structure of global BOLD signals under both free breathing and under a 'clamped' CO2 condition, where end-tidal CO2 (PETCO2) was 'clamped' to the average level of each participant (Golestani & Chen, 2020).

The spatial structure of the global BOLD signal was estimated with the spatial weights of the first principal component and compared across free breathing and 'clamped' CO2 conditions (**Figure 2C**). The spatial structure of global BOLD signals is nearly identical between free breathing and clamped CO2 conditions (correlation r = 0.95 of the spatial weights between the two conditions). Further, global BOLD signals are similarly present in both conditions, as reflected in the explained variance estimates of the first principal component between the two conditions ($PC1_{free}$ $r^2 = 0.28$; $PC1_{clamped}$ $r^2 = 0.25$; **Supplementary Figure 10**). Consistent with a previous report comparing overall time-lag structure of BOLD signals between clamped and free breathing conditions (Kish et al., 2023), we found that the spatiotemporal structure of global BOLD signals was similarity maintained in clamped CO2 conditions (**Supplementary Figure 4**).

Discussion

This study characterizes a large-scale, ubiquitous pattern of synchrony between global brain signals and the ANS in humans. Across multiple independent samples of multi-modal fMRI, EEG and peripheral physiology resting-state recordings, our findings provide evidence of a low-frequency (0.01-0.1Hz), low-dimensional synchrony spanning the brain and body. These fluctuations are widespread across the body and entire nervous system, involving the brain, heart, lungs, exocrine and smooth muscle systems. These co-fluctuations were linked to changes in arousal state induced via deep breathing and sensory stimulation, as well as spontaneous fluctuations in arousal observed during sleep. Further, the global hemodynamic component of these co-fluctuations is not fully explained by accompanying respiratory-driven fluctuations in arterial CO2.

The co-fluctuations between global brain activity and peripheral physiology exhibit a stereotypical sequence. The initial positive increase in global BOLD and broadband EEG power is accompanied by roughly simultaneous increases in heart rate, peripheral vascular tone and broadband EEG power. The increase in heart rate and the subsequent decrease is consistent with gating of parasympathetic outflow (via the vagus nerve) during inspiration and its relaxation during exhalation, known as respiratory sinus arrhythmia (Yasuma & Hayano, 2004). The increase in peripheral vascular tone, as reflected by the drop in PPG amplitude and low-frequency PPG (0.01-0.1 Hz) signal, is indicative of vasoconstriction of peripheral blood vessels by sympathetic outflow (Khoo & Chalacheva, 2019). While pupil diameter and tonic skin conductance signals were only recorded in resting-state conditions, impulse response analyses (**Figure 1**) provides potential insights into their dynamics during evoked conditions. For

example, a small positive increase in pupil dilation occurs shortly before the overshoot of the global BOLD signal, consistent with inhibition of parasympathetic-mediated outflow to the iris constrictor muscles and excitation of sympathetic-mediated outflow to the iris dilator muscle (Marumo & Nakano, 2021), followed by a larger decrease in pupil dilation several seconds later, consistent with decreased sympathetic outflow. Tonic skin conductance peaks around the same time as the overshoot of the global BOLD signal, consistent with sympathetic-mediated increases in sudomotor activity.

We observed that experimentally-induced or spontaneous variance in ANS activity reproduces the same sequence of physiological and global hemodynamic activity observed at rest. Here, experimental manipulation of ANS activity was performed through cued deep breathing and sensory stimulation, but other autonomic challenges may produce a similar effect. For example, performance of the Valsalva maneuver in an MRI scanner produced a similar magnitude change of global BOLD signal change as that observed with breath holding (Wu et al., 2015). While smaller in magnitude, intermittent auditory-cued button responses reproduced the same sequence of physiological and global hemodynamic activity observed during deep breathing. The same spatiotemporal sequence was also observed around K-complex onsets during sleep, consistent with a previous report (Özbay et al., 2019) that found increased global BOLD-physiological coupling around K-complex onsets during the NREM2 sleep stage. This finding is also largely consistent with findings that the amplitude of global BOLD signals is increased during states of low vigilance (drowsiness, early sleep stages) (Falahpour et al., 2018; Wong et al., 2013). Together, these observations suggest that 1) this phenomena is not restricted to respiratory-specific mechanisms and 2) the link between deep breathing and global BOLD dynamics is mediated by the ANS (sympathetic) and its projections to central autonomic nuclei in the brainstem or cerebral vasculature.

These findings shed light on the ongoing debate over the origin of global BOLD fluctuations in the fMRI community (Liu et al., 2017; Murphy & Fox, 2017). An often-cited causal mechanism for the origin of global BOLD signals is respiratory-driven changes in arterial CO2 concentration (Wise et al., 2004). Changes in breathing depth and rate and respiratory reflexes occur frequently in resting-state fMRI scanning sessions. Power and colleagues (Lynch et al., 2020; Power et al., 2017, 2019) have demonstrated that subjects in resting-state fMRI recording conditions exhibit frequent breathing changes and reflexes (e.g. ‘yawns’ and ‘sighs’). These behaviors likely induce variation in arterial CO2 concentration in the cerebral vasculature, thereby increasing/decreasing cerebral blood flow. Our findings that the topography and spatiotemporal structure of global BOLD fluctuations is maintained under experimental suppression of PETCO2 fluctuations suggest that the origin of global BOLD fluctuations are unlikely to arise primarily from arterial CO2 fluctuations.

Another possibility is an increase in systemic oxygenation levels of the cerebral vasculature via an increase in respiratory rate and depth (Zhang et al., 2019). While this possibility cannot be excluded, the observation of the same physiological dynamics in response to spontaneous changes in ANS activity suggests this is not the sole driver of our findings. However, the global BOLD response to deep breathing was much stronger in amplitude

compared with K-complex onsets and sensory stimulation, suggesting that systemic oxygenation fluctuations could act as a gain modulator of the response.

Our findings of a tight coupling between global BOLD and ANS-mediated physiological dynamics, and their reproduction by experimental or spontaneous variation in autonomic outflow, provide evidence that the ANS (primarily the sympathetic nervous system) is the key driver of global BOLD signals. Our results leave open the proximal causal mechanism by which ANS activity and global BOLD signals are linked. Such a link may be direct, via sympathetic-innervation of the cerebral vasculature. Cerebral blood vessels are profusely innervated by α-adrenergic receptors and may play a role in cerebral autoregulation (Koep et al., 2022), but the extent of their vasoconstrictive effect on cerebral blood vessels, and thereby BOLD signals in the brain, is controversial (van Lieshout & Secher, 2008). The autoregulatory contribution of the sympathetic nervous system to cerebral blood flow may be most prominent during abrupt or rapid changes in blood pressure (Claassen et al., 2021) as would be the case in a sudden increase in global cerebral blood flow. Further, some evidence suggests that sympathetic regulation of cerebral blood flow may be most prominent at frequencies higher than 0.05Hz (Hamner et al., 2010), around the frequency range of fluctuations in global BOLD observed in this study. However, a potential vasoconstrictive effect on cerebral blood flow would only explain the decrease in global BOLD signal following the overshoot phase (~4s post onset). In such a scenario, the transient increase in cerebral blood flow in the early overshoot phase would activate a protective attenuation via sympathetic vasoconstriction to increased perfusion pressure.

The early peak or overshoot phase (~4s) of the physiological response may be mediated by an indirect, neurogenic ANS pathway. The timing of the global BOLD peak is within the range of the time to peak (~4 - 6s) of the canonical hemodynamic response to a brief stimulus impulse (Buxton et al., 2004). Consistent with local field potential and surface EEG studies in animal and human subjects (Ito et al., 2014; Kluger & Gross, 2021; Shams et al., 2021; Zelano et al., 2016), our study found an increase in broadband EEG power peaking at a ~4s time lag (**Figure 2**), though others have found distinctive dynamics in the alpha band (Shams et al., 2021). However, the simultaneous timing of the early overshoot of the hemodynamic response with peaks of broadband EEG power suggests that these fluctuations are not a causal source of the early overshoot, given the conventional delay in neurovascular coupling (~4-6s). Nevertheless, the alignment of the early overshoot of the hemodynamic response to the canonical hemodynamic response and modulation of broadband EEG power suggests that a neurogenic mechanism is one potential candidate for the early overshoot. A potential neurogenic mechanism may be mediated by noradrenergic brainstem nuclei (e.g. locus coeruleus) that project diffusely to the cortex (Samuels & Szabadi, 2008).

The finding that this brain-body physiological response was most effectively induced by an experimentally-cued deep inhalation underscores the therapeutic significance of slow, deep breathing for stress and anxiety (Ashhad et al., 2022; Zaccaro et al., 2018). Our findings suggest that respiratory-driven changes in affect and mood may arise from two pathways - a direct, neurogenic pathway reflected by global hemodynamic and EEG fluctuations, and an

indirect pathway via ANS afferent activity from peripheral organs (e.g. exocrine, cardiovascular systems). The former could be partially mediated by direct projections between breathing pattern generators in the brainstem and ascending arousal system nuclei (Yackle et al., 2017). The latter would constitute a visceral sensory feedback mechanism from organs involved in the stress response. While the pathways that sustain this low-frequency brain-body synchrony remain under experimental investigation, the widespread nature of this synchrony suggests that its promotion or suppression could have significant therapeutic applications.

Acknowledgements
BTTY is supported by the NUS Yong Loo Lin School of Medicine (NUHSRO/2020/124/TMR/LOA), the Singapore National Medical Research Council (NMRC) LCG (OFLCG19May-0035), NMRC CTG-IIT (CTGIIT23jan-0001), NMRC STaR (STaR20nov-0003), Singapore Ministry of Health (MOH) Centre Grant (CG21APR1009), the Temasek Foundation (TF2223-IMH-01), and the United States National Institutes of Health (R01MH120080 & R01MH133334). Any opinions, findings and conclusions or recommendations expressed in this material are those of the authors and do not reflect the views of the Singapore NMRC, MOH or Temasek Foundation. CC acknowledges support from NIH grants RF1MH125931 and P50MH109429.

Supplementary Materials

Supplementary Movies

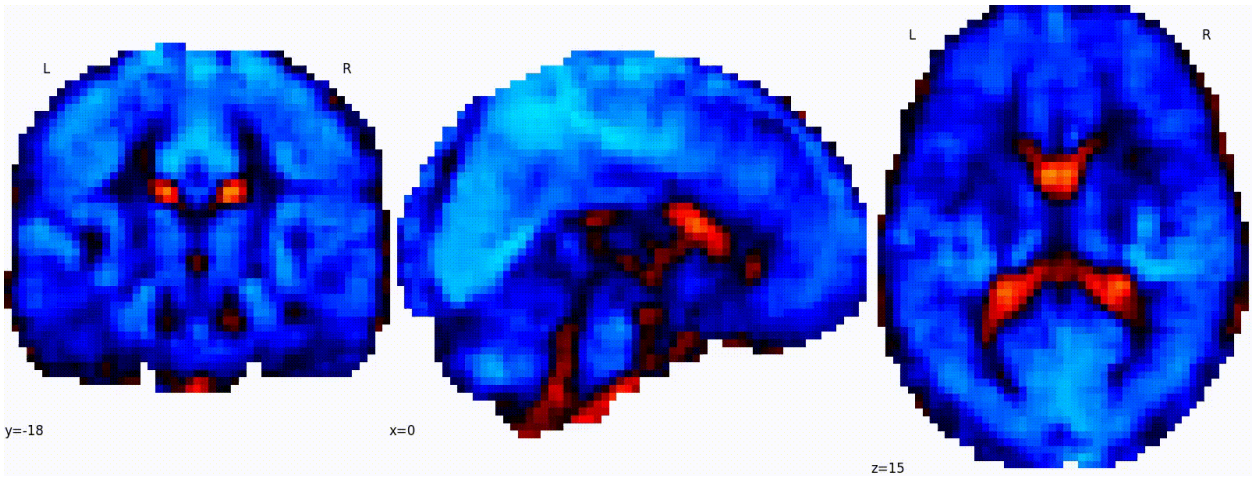

Supplementary Movie 1. **Temporal Reconstruction of CPC1 in ME-REST Dataset.**

Supplementary Tables

Dataset	Sample	Physio Signals Used	Source	Sample Size	Number of Sessions	Age Range	Sex (F)
ME-REST	Full	EEG, Respiration, PPG	Goodale et al. (2021). *ELife*. https://doi.org/10.7554/eLife.62376	11	15	21-35	6
ME-TASK	Full	EEG, Respiration, PPG	Unpublished dataset; https://www.cchanglab.net/	6	9	22-57	4
ME-TASK-CUE	Full	EEG, Respiration, PPG	Goodale et al. (2021). *ELife*. https://doi.org/10.7554/eLife.62376	12	12	21-33	6
ME-REST-SUPP	Subset	Respiration, PPG	https://openneuro.org/datasets/ds003592/versions/1.0.11 **OpenNeuro Accession Number:** ds003592 **Version:**	87	165	18 - 34	58

			1.0.11				
HCP-REST	Subset	Respiration, PPG	https://www.humanconnectome.org/	30	30	22-37	17
NKI-TASK	Subset	Respiration, PPG, Skin Conductance	http://fcon_1000.projects.nitrc.org/indi/enhanced/	50	50	15-45	30
NKI-REST	Subset	Respiration, PPG, Skin Conductance	http://fcon_1000.projects.nitrc.org/indi/enhanced/	50	50	18-45	33
NATVIEW-REST	Full	EEG, Pupillometry	(Telesford et al., 2023)	21	33	22-51	10
YALE-REST	Full	Pupillometry	https://openneuro.org/datasets/ds003673/versions/2.0.1 **OpenNeuro Accession Number:** ds003673 **Version:** 2.0.1	27	54	21-37	16
Clamped CO2	Full	N/A	(Golestani & Chen, 2020)	13	13	18-32	9

Supplementary Table 1. **Dataset Details and Demographics.** Details (manuscript label, signals recorded, reference) and demographics (sample size, age range, sex) for datasets used in this study. Note, demographics are based on the dataset sample after the quality control stage.

Supplementary Figures

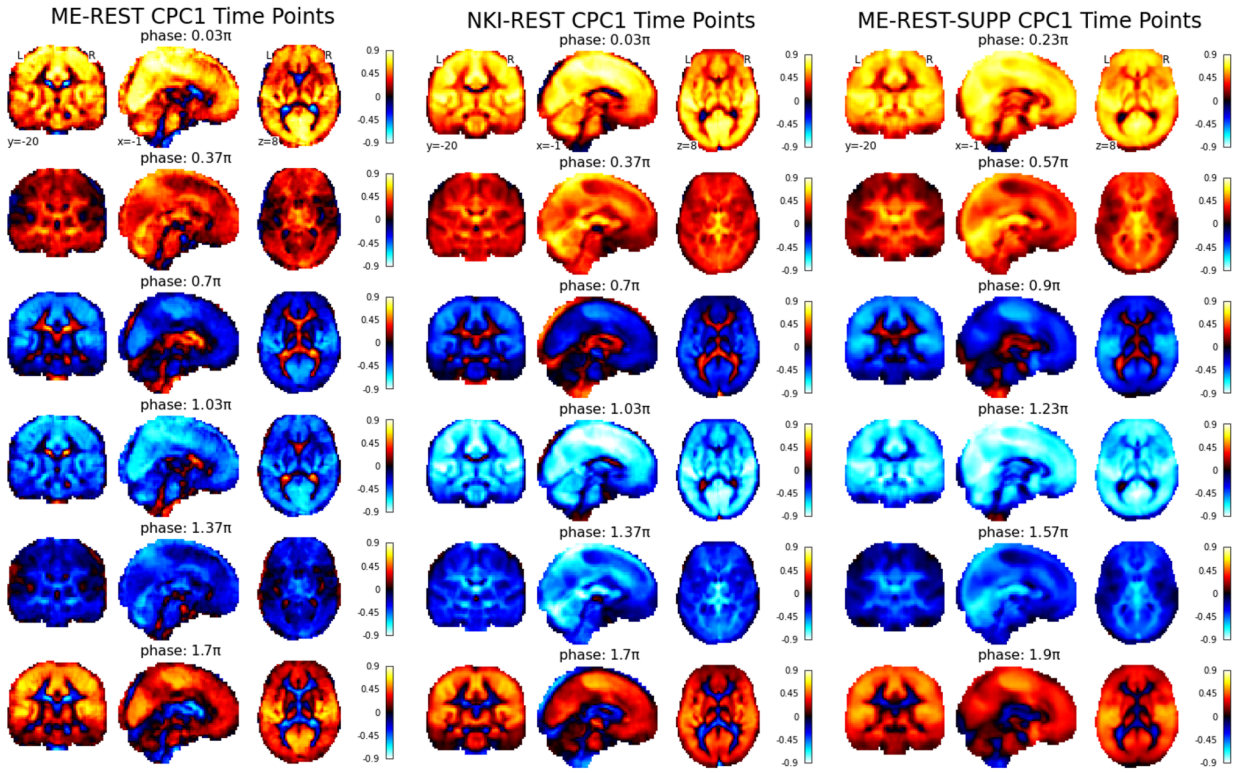

Supplementary Figure 1. **Spatiotemporal Dynamics of Global BOLD Signals.** Temporal reconstruction of the first complex principal component (CPC1) of three resting-state fMRI datasets (ME-REST, NKI-REST, ME-REST-SUPP). Complex PCA (CPCA) on other resting-state datasets (HCP-REST, NATVIEW-REST, YALE-REST) yielded similar results, and are not included here for space. As shown in previous work, the first principal component from PCA and complex principal component from CPCA extract the global BOLD signal, with CPCA yielding a spatiotemporal representation of the global BOLD signal (Bolt et al., 2022). The time course of a complex principal component is represented in complex numbers, and its phase can be extracted (measured in radians). A temporal reconstruction of the complex principal component can be constructed via averaging of the original BOLD signals (in voxel space) at similar phase values. We selected six equally spaced phase values to display the spatiotemporal dynamics of the global BOLD signal. Time moves in the positive direction, such that increasing phase values move forward in time. A consistent spatiotemporal pattern is observed across datasets: a global increase in BOLD signals in the gray and white matter followed by a propagation of BOLD signals to large draining veins and ventricles, and then a global decrease in BOLD signals.

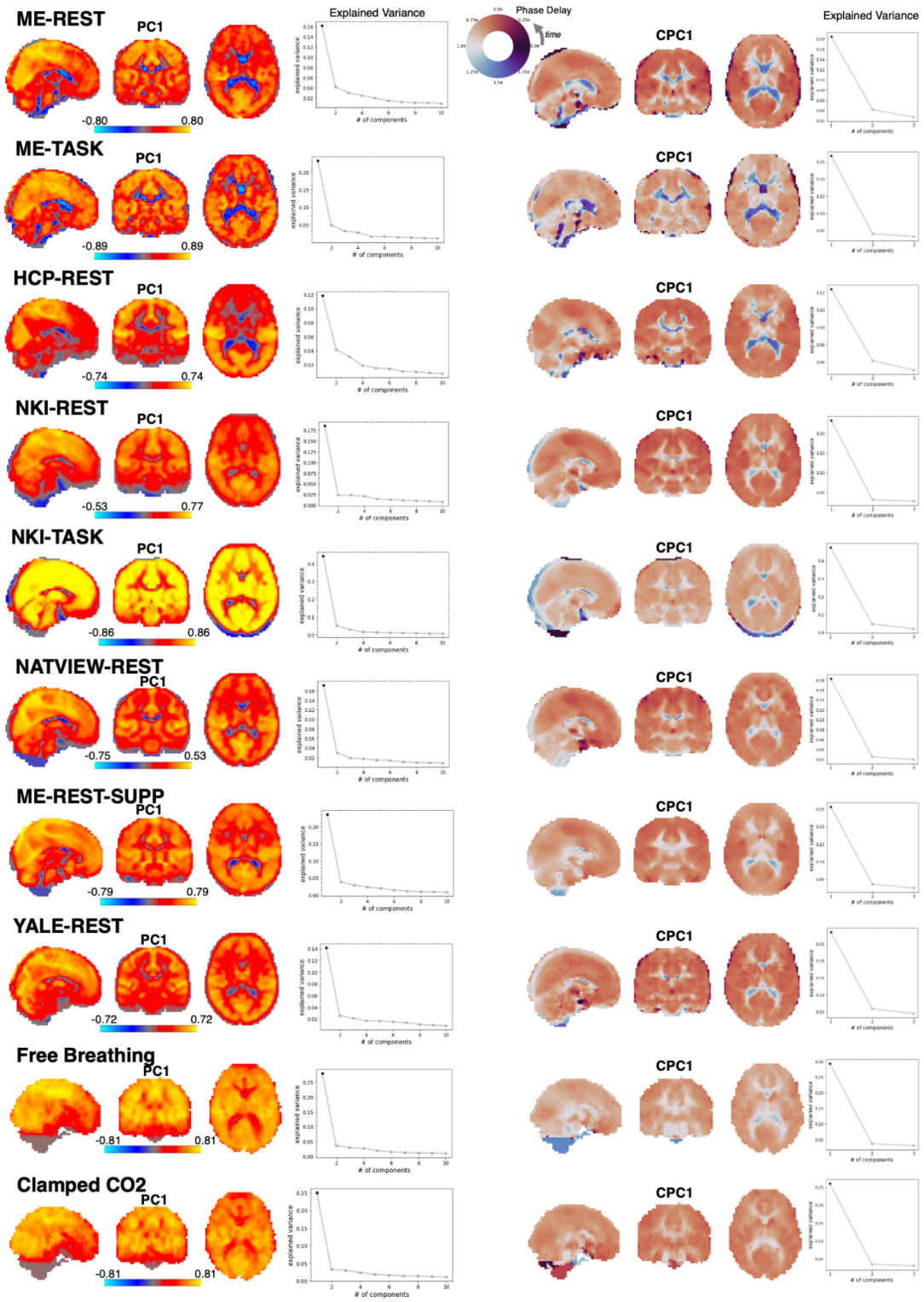

Supplementary Figure 2. **First Principal Component and Complex Principal Component Across Datasets.** Spatial weights of the first principal component (PC1; left) and phase delay maps of the first complex principal component (CPC1; right) across all datasets used in this study. Explained variance plots (Scree plots) are displayed to the right of each brain map displaying the explained variance by the

first and subsequent principal components. The phase delay map of the first complex principal component encodes the time-delay (in radians) between voxels within the component. Because phase delay is measured in radians (0 to 2pi), they are displayed with a circular color map.

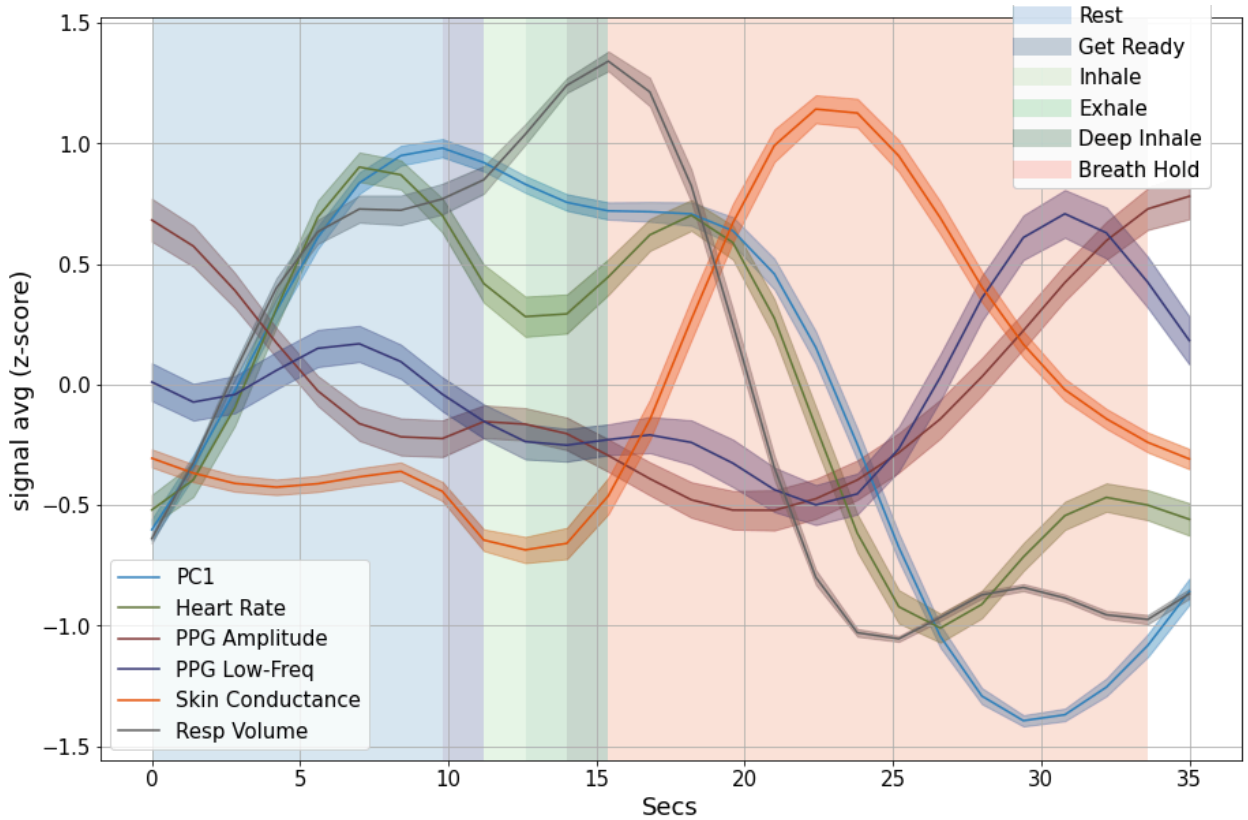

Supplementary Figure 3. **NKI-Breath Hold Task.** Physiological trial averages for a full block of the paced inhalation/breath hold task (NKI-TASK). The paced breathing/breath-hold task was a block design consisting of a fixed sequence of rest (10s), a cue (2s) followed by two deep inhalations (6s), and a breath-hold (18s), immediately followed by another sequence. Time points in separate blocks are shaded to distinguish activity in each block: rest (10s duration; blue), 'get ready' cue (2s; dark blue), inhalation (2s; light green), exhalation (2s; medium green), deep inhalation (2s; dark green) and breath hold (18s; red).The physiological dynamics of the paced breathing/breath hold task (NKI-TASK) are more complex than those observed in response to isolated deep inhalations (**Figure 2A**). For example, large increases in respiratory volume are observed during the paced inhalation exercise before the breath hold and the 'rest' blocks that precede the paced inhalation exercise, due to their placement immediately after the breath hold. The timing of the large amplitude peak of global BOLD signals in the rest period (~10s) and following the deep inhalation block (19s) are consistent with the timing of the respiration response peak observed to isolated deep inhalations (**Figure 2A**). Consistent with the response to isolated deep inhalations, an increase in heart rate is observed around the time of the global BOLD peak, shortly followed by peripheral vasoconstriction. In addition, a large amplitude response in skin conductance is observed around the same time as peripheral vasoconstriction. The trough of the global BOLD response, along with peripheral vasodilation, occurs in the latter half of the breath hold block, consistent with the peak-to-trough timing observed in deep inhalations.

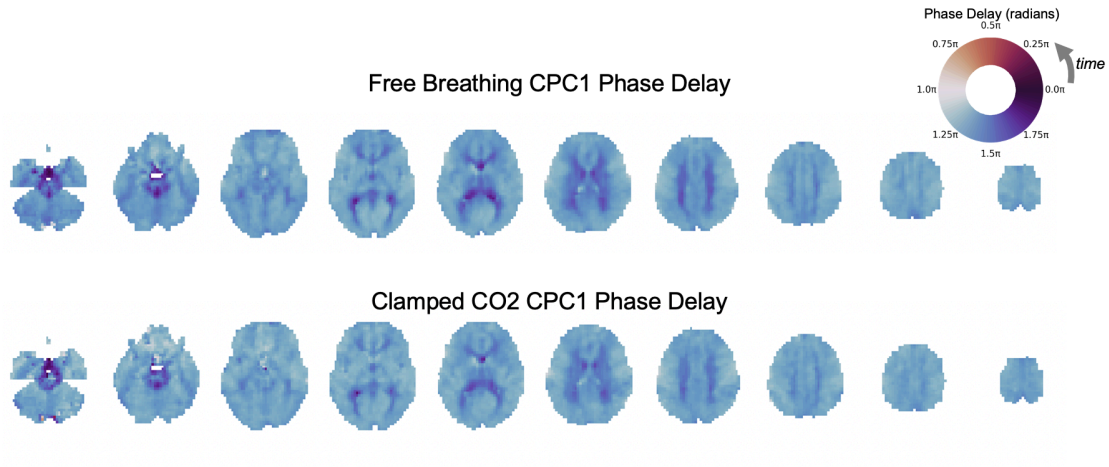

Supplementary Figure 4. **First Complex Principal Component Phase Delay in Free Breathing and Clamped CO2 Conditions.** Phase delay maps of the first complex principal component (CPC1) computed from BOLD time courses in free breathing and clamped CO2 conditions. The phase delay map of the first complex principal component encodes the time-delay (in radians) between voxels within the component. Because phase delay is measured in radians (0 to 2pi), they are displayed with a circular color map. As can be observed from the brain maps, the distribution of phase delay values across the brain is highly similar across free breathing conditions and clamped conditions.

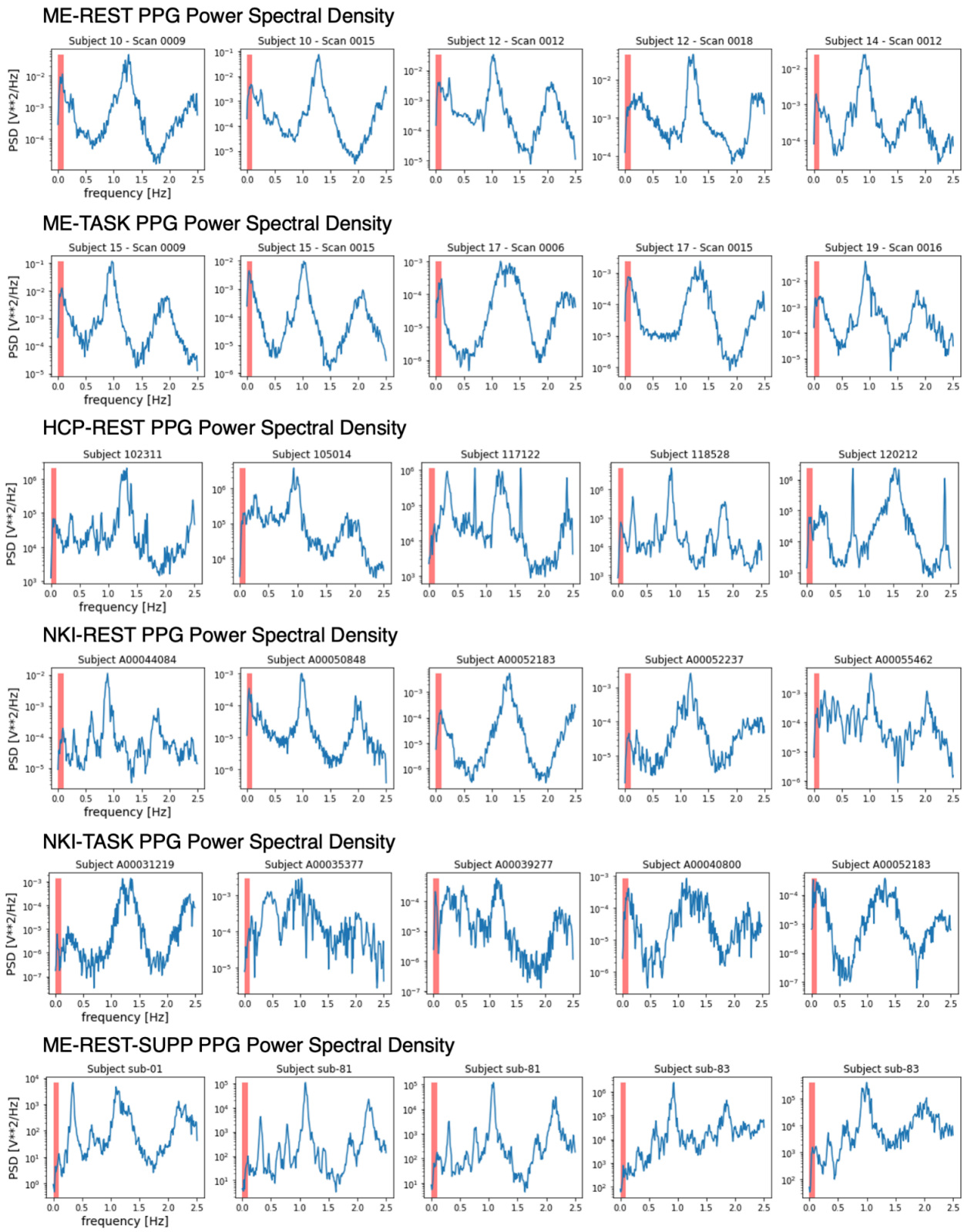

Supplementary Figure 5. **Power Spectral Density of Pulse Oximeter Time Courses Across Datasets.** Power spectral density estimates (0 to 2Hz) from pulse oximeter (PPG) signals displayed for all datasets

that acquired PPG signals. The power spectral density estimates are log-transformed on the y-axis. All PPG signals were resampled to a 5Hz sampling rate before power spectral density estimation. The power spectral density estimates were estimated using Welch's method (window length = 500 time points, window overlap= 50 time points).

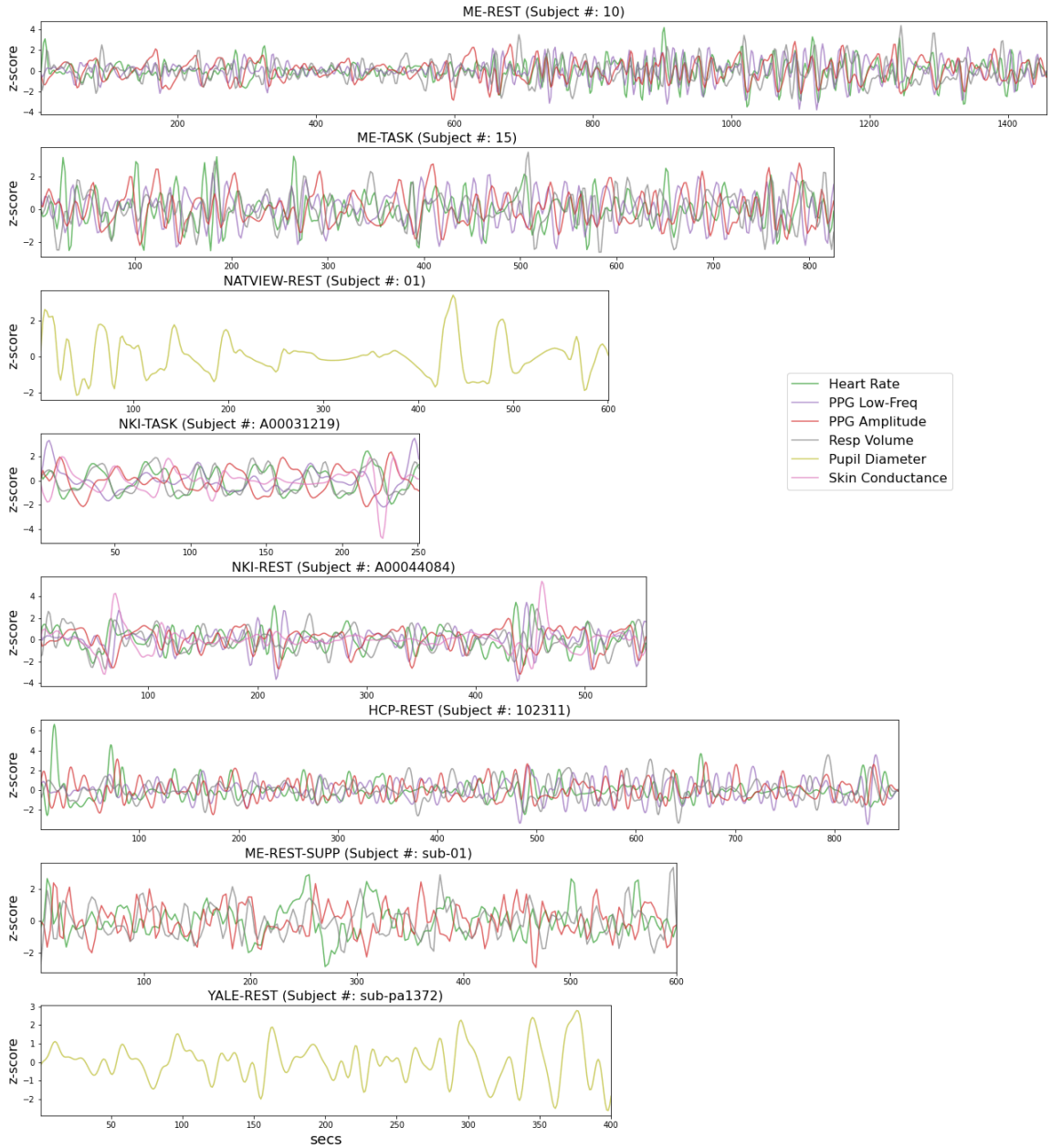

Supplementary Figure 6. **Physiological Time Series from Example Subjects.**

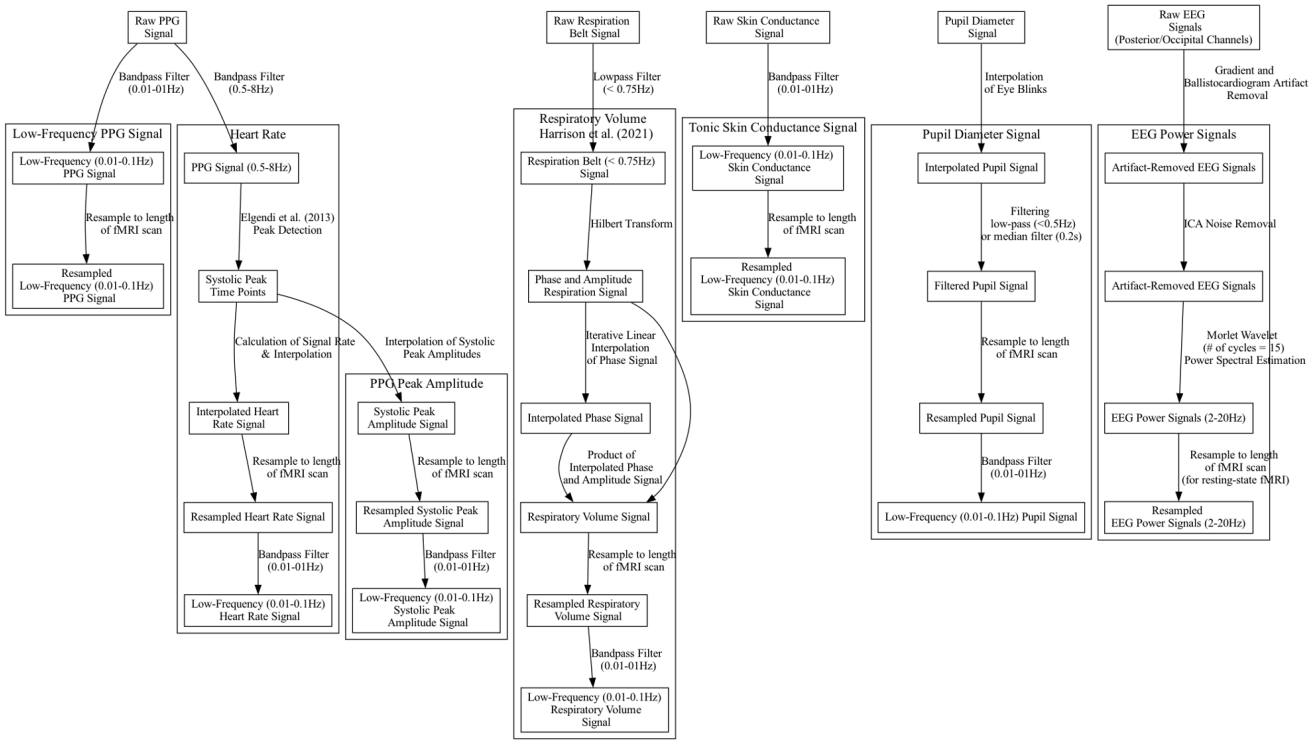

Supplementary Figure 7. **Electrophysiological Signal Preprocessing Pipeline.**

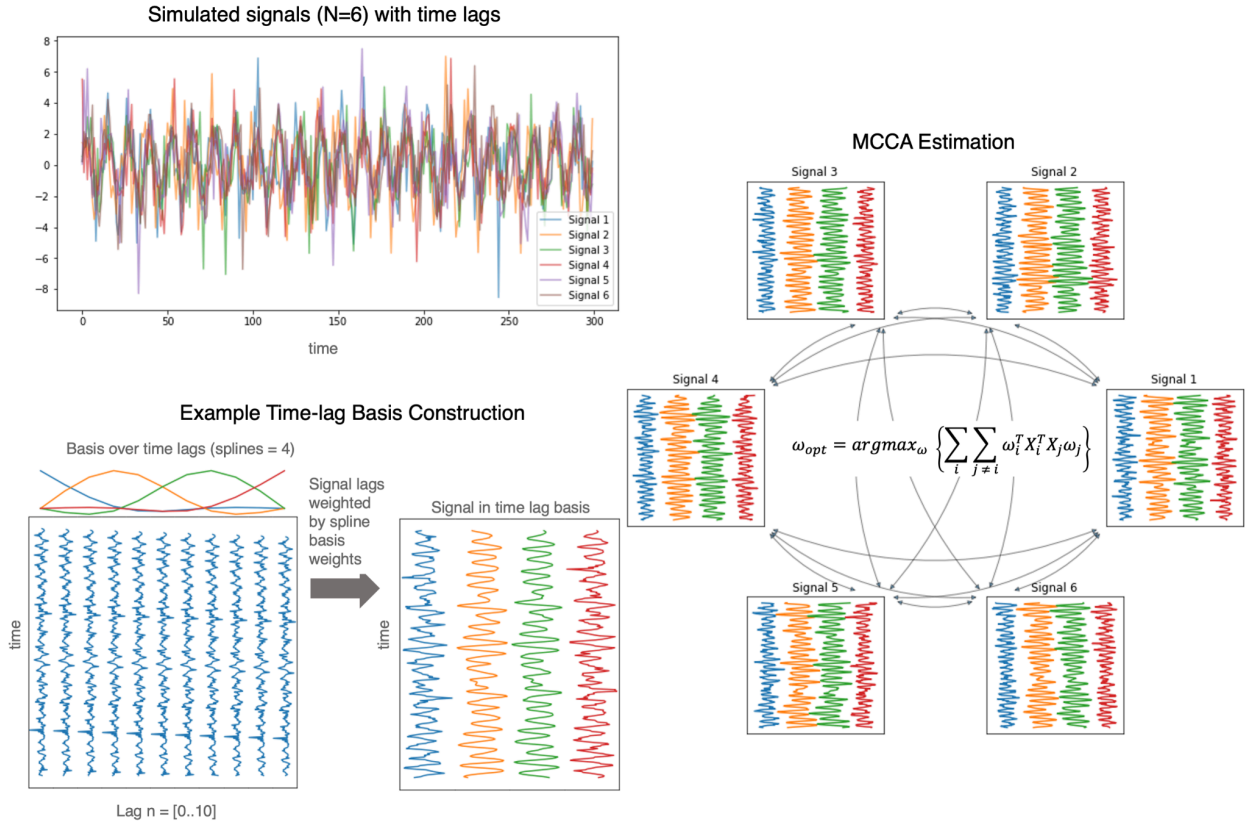

Supplementary Figure 8. **Illustration of Multiset Canonical Correlation Analysis.**

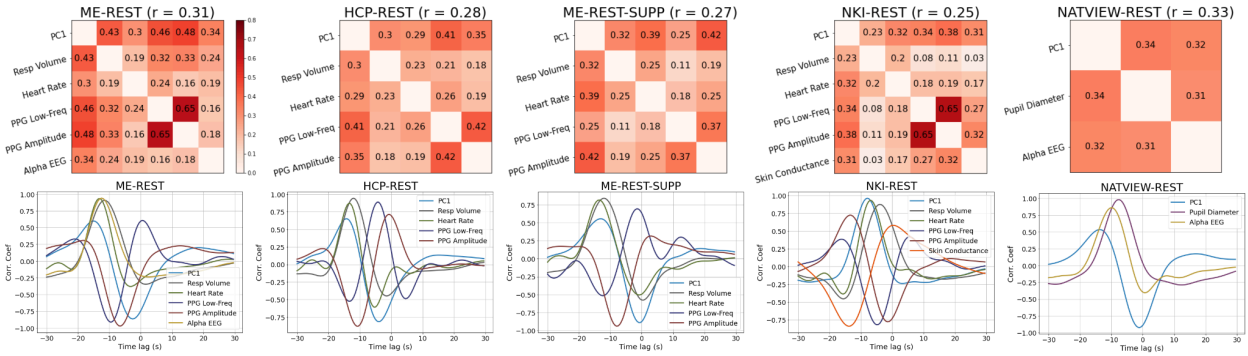

Supplementary Figure 9. **MCCA of Resting-State Datasets and Cross-Correlations. Top panel:** The pairwise correlations (top) between all physiological signals (including the global BOLD signal; PC1) in the first canonical component of the MCCA analysis and their time lags (bottom) for five resting-state datasets, as displayed in **Figure 1**. The average pairwise correlation is displayed beside the title of each correlation matrix. **Bottom panel:** To extract timing information between the signals in this low-dimensional space, we cross-correlated each physiological signal with its projection onto the first canonical component**.** The cross-correlations between each physiological signal and its projection onto the first canonical component are displayed in the bottom panel, where each signal is displayed in a different color. Comparison of the relative timing between peaks of the cross-correlation curves across

physiological signals provides the lead-lag relationships between signals within the first canonical component of MCCA.

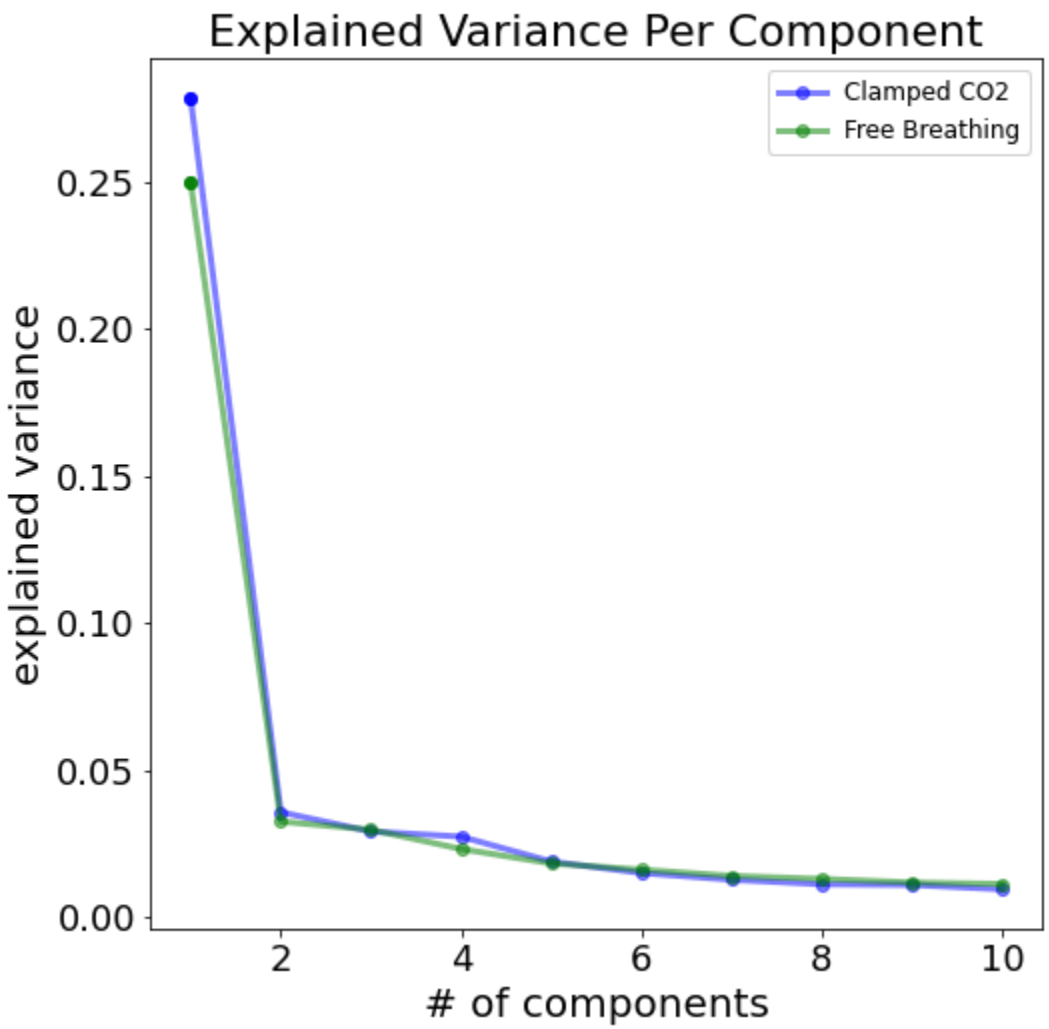

Supplementary Figure 10. **Scree Plot of Eigenvalues for Clamped CO2 and Free Breathing Conditions.** A scree plot of eigenvalues of the first ten components from PCA estimated from the free breathing (green) and 'clamped' CO2 (blue) condition. As can be observed, the spatial distribution of the global BOLD signal is maintained when variations of CO2 are experimentally suppressed. More generally, the low-dimensional spatial structure of BOLD time courses between the two conditions, as reflected in the scree plot, is similar between the two conditions.

Methods and Materials

Participants and Data Acquisition

Ten datasets were analyzed in this study: 1) a simultaneous EEG/multi-echo resting-state fMRI dataset (ME-REST), 2) a simultaneous EEG/multi-echo respiration task fMRI dataset (ME-TASK), 3) a simultaneous EEG/multi-echo reaction time task fMRI dataset (ME-TASK-CUE) 4) a multiband accelerated single-echo resting-state fMRI dataset from the Human Connectome Project (Van Essen et al., 2013) (HCP-REST) , 5) a multiband accelerated single-echo fMRI dataset from the enhanced Nathan Kline Institute (NKI) - Rockland Sample (Nooner et al., 2012), including a resting-state (NKI-REST) and 6) respiration task (NKI-TASK) , 7) a supplementary multi-echo fMRI resting-state dataset (Spreng et al., 2022) (ME-REST-SUPP), 8) a multiband accelerated single-echo resting-state fMRI dataset with simultaneous pupillometry from Yale University (Lee et al., 2022) (YALE-REST), 9) a simultaneous EEG/single-echo resting-state fMRI dataset from NKI (Telesford et al., 2023) (NATVIEW-REST), 10) a multiband accelerated single-echo resting-state fMRI dataset recorded under a free breathing condition and a PETCO2 condition clamped to the average PETCO2 for each participant. Dataset details and demographics are presented in **Supplementary Table 1**.

ME-REST, ME-TASK, ME-TASK-CUE Data

Simultaneous multi-echo fMRI-EEG eyes-closed resting-state scans (ME-REST) were acquired from 11 healthy, right-handed participants (6 females, mean age = 25.9 years). All subjects provided written informed consent, and human subjects protocols were approved by the Institutional Review Boards of the National Institutes of Health and Vanderbilt University. Two resting-state sessions were recorded for four of the subjects, creating a total of 15 scans. Simultaneous multi-echo fMRI-EEG respiration task scans (ME-TASK) were acquired under the same acquisition protocol for six healthy, right-handed participants (4 females, mean age = 30.5). Two task sessions were recorded for three of the subjects, creating a total of 9 scans. The respiration task experimental design consisted of a sparse event-related design with instructions to the participants to take a deep breath in response to an auditory cue (a constant tone). The interstimulus interval (ISI) between auditory cues was randomly jittered between the range of 60.55 and 131.25 sec. Auditory cue timing was consistent across scans. One participant overlapped between the resting-state and respiration task sessions. Simultaneous multi-echo fMRI-EEG reaction time task scans (ME-TASK-CUE) were acquired under the same acquisition protocol for twelve healthy, right-handed participants (6 females, mean age = 25.6 years). The reaction time task experimental design consisted of a sparse event-related design with instructions to the participants to press a button in response to an auditory cue. For some subjects (N=5), the ISI between auditory cues was set to 35s±6s, and for the rest (N=7) the ISI was randomly jittered between 8 and 89 secs. Nine participants overlapped between the resting-state and reaction time task sessions.

Detailed MRI/EEG acquisition parameters are provided in Goodale et al. (2021). Briefly, anatomical T1-weighted structural and multi-echo EPI BOLD scans were collected on a 3T Siemens Prisma scanner with a Siemens 64-channel head/neck coil. The multi-echo EPI sequence was acquired with TR = 2100 ms, echo times = 13.0, 29.4, and 45.7 ms, flip angle = 75 degrees, and voxel size = 3mm isotropic. The duration of the resting-state scan was 24.5 minutes, corresponding to a total of 700 volumes. The duration of the respiration task scan was slightly variable (14-15 minutes across subjects), corresponding to a total of 400-435 volumes, depending on the subject. Simultaneous scalp EEG (sampling rate = 5 kHz) was acquired during the resting-state and respiration task using a 32-channel MR-compatible system. Photoplethysmography (PPG) and respiration belt signals (sampling rate: 2 kHz) were acquired during both the resting-state and respiration task sessions. The PPG transducer was placed on the left index finger. MRI scan triggers were recorded along with EEG and physiological signals for data synchronization.

HCP-REST Data

We analyzed eyes-open resting-state fMRI EPI scans from the HCP S1200 release. We randomly selected 30 unrelated, healthy young adults (ages 22–37; 17 females) for our study with high quality physiological recordings (confirmed through visual inspection; see note below on quality control procedure). We chose 30 subjects for two reasons: 1) analyses were found to be replicable at small sample sizes (< 15 subjects) for the HCP dataset, and 2) the length of the scans (length of scan: 1200 time points) imposed significant computational challenges. Detailed MRI/Physio acquisition parameters are provided in Smith et al. (2013). Briefly, resting-state fMRI scans were collected on Siemens 3T Tim Trio scanners with a multiband (factor of 8) accelerated EPI sequence with the following parameters: TR: 720ms, TE = 33.1ms, flip angle = 52 degrees, and voxel size= 2mm isotropic. Resting-state fMRI data was collected over two consecutive days for each subject and two sessions, each consisting of two 15-minute runs, amounting to four resting-state sessions per subject. Within a session, the two runs were acquired with opposite phase encoding directions: L/R encoding and R/L encoding. A single 15 min scan from each participant on the first day of scanning was selected. We balanced the number of L/R and R/L phase encoding scans across our participants (n=15 for L/R direction) to ensure results were not biased by acquisition from any given phase encoding direction. Photoplethysmography (PPG) and respiration belt signals (sampling rate = 400 Hz) were simultaneously acquired with resting-state EPI scans along with MRI scan triggers for data synchronization.

NKI-REST and NKI-TASK Data

We analyzed resting-state and task-fMRI breath-hold EPI scans, and high-resolution anatomical T1w images from the enhanced Nathan Kline Institute (NKI) Rockland sample. We randomly selected 50 adult subjects with high-quality physiological recordings (confirmed through visual inspection; see note below on quality control procedure) independently for each dataset (NKI-REST: ages 18-45, 33 females; NKI-TASK: ages 15-45, 30 females). Twenty subjects overlapped between the two datasets. A single respiration task session was recorded

per participant with a 1400ms TR. Two multi-band accelerated resting-state sessions (TR: 1400ms and TR: 650ms) were collected per participant. We selected the 1400ms (TR) acquisition for consistency with the respiration task. Detailed acquisition parameters are provided on the Enhanced NKI-Rockland webpage (http://fcon_1000.projects.nitrc.org/indi/enhanced/index.html). Briefly, resting-state and breath hold fMRI scans were collected on a Siemens 3T Tim Trio scanner with a multiband (factor of 4) accelerated EPI sequence with the following parameters: TR = 1400ms, TE = 30ms, flip angle = 65 degrees, voxel size = 2mm isotropic. The duration of the resting-state scan was 10 minutes. The respiration task was a block design with the following sequence: 1) a 10-sec rest, 2) a 2-sec visual stimulus indicating the start of the trial (text: 'Get Ready'), 3) a 2-sec inhalation, 4) a 2-sec expiration, 5) a 2-sec deep inhalation, and 5) a breath hold for 18 secs. This sequence was repeated seven times, for a total duration of 4.5 minutes. PPG signals (recorded from the tip of the index finger), skin conductance (galvanic skin response; recorded from the hand), and respiration belt signals were simultaneously acquired with EPI scans along with MRI scan triggers for data synchronization.

ME-REST-SUPP Data

As a supplementary multi-echo fMRI dataset to confirm findings from the ME-REST and HCP-REST datasets, we analyzed eyes-open resting-state data from the neurocognitive aging data release (Spreng et al., 2022). We selected 87 young adults with high quality physiological recordings (confirmed through visual inspection; see note below on quality control procedure) (ages 20 - 34, 20 females). Each participant performed two resting state fMRI sessions during the study visit. Detailed MRI acquisition parameters are provided in Spreng et al. (2022). Briefly, anatomical T1-weighted structural and multi-echo EPI BOLD-fMRI scans were collected on a 3T GE Discovery MR750 scanner with a 32-channel head coil. The multi-echo EPI sequence was acquired with TR = 3000 ms, echo times = 13.7, 30, and 47 ms, flip angle = 83 degrees, and voxel size = 3mm isotropic. The duration of the resting-state scan was 10 minutes, corresponding to a total of 204 volumes. Photoplethysmography (PPG) and respiration belt signals (sampling rate: 40 or 50 Hz) were acquired during the session.

YALE-REST Data

For analysis of pupillometry signals, we analyzed eyes-open resting-state fMRI data from the Yale Resting-State Pupillometry/fMRI dataset (Lee et al., 2022) via OpenNeuro (Markiewicz et al., 2021; OpenNeuro Accession Number: ds003673). 24 of the 27 participants were selected for analysis based on quality control of the pupil recordings (ages 21 - 37, 16 females). Both resting-state fMRI sessions collected during the study visit were used. Detailed MRI acquisition parameters are provided in Markiewicz et al. (2021). Briefly, anatomical T1-weighted structural and single-echo, multiband EPI BOLD-fMRI scans were collected on a MAGNETOM Prisma MRI scanner. The single-echo, multiband EPI sequence was acquired with TR = 1000ms, TE = 30ms, multiband acceleration factor = 5, flip angle = 55 degrees and voxel size = 2mm. The duration of each resting-state scan was 6 minutes and 50s. Simultaneous eye-tracking and pupil dilation was recorded using a MR-compatible infrared EyeLink 1000 Plus eye-tracking system

with a 1000Hz sampling rate. We used minimally preprocessed pupil data provided by the authors for analysis (see details below).

NATVIEW-REST Data

To replicate EEG and pupillometry associations, we analyzed eyes-open resting-state data with simultaneous EEG-fMRI-pupillometry recordings from NKI (Telesford et al., 2023). We selected 21 of 22 total subjects based on visual inspection of the minimally processed pupil diameter recordings (ages 22-51, 10 females). The resting-state scans were approximately 10 minutes in duration (288 volumes) and were collected as part of a larger naturalistic viewing experiment with several visual and movie watching scans. For some subjects (N=12), two resting-state sessions were collected, and both were used in our analysis. Detailed MRI/EEG acquisition parameters are provided in Telesford et al. (2023). Briefly, anatomical T1-weighted structural and single-echo EPI BOLD scans were collected on a 3T Siemens TIM Trio scanner with a 12-channel head coil. Resting-state EPI sequences were acquired with TR=2100ms, TE=2500ms, flip angle = 60 degrees, voxel size= ~3.5mm isotropic.

Simultaneous scalp EEG (sampling rate = 5 kHz) was collected using a customized 61-channel MR-compatible cap, including two electrooculogram (EOG) channels (above and below the left eye) and one electrocardiography (ECG) channel placed on the back. As with the *YALE-REST* dataset, simultaneous eye-tracking and pupil dilation was recorded using an MR-compatible infrared EyeLink 1000 Plus eye-tracking system with a 1000Hz sampling rate. We used minimally preprocessed pupil data provided by the authors for analysis (see details below). Respiratory time courses were also collected with a respiratory belt, but due to data quality issues were not included in our analysis.

Free Breathing and 'Clamped' CO2 Data

To determine the effect of spontaneous variation in arterial CO2 produced by changes in respiratory depth/rate on global BOLD dynamics, we analyzed resting-state fMRI data from 13 participants (ages 18 - 32, 9 females) collected during free breathing and clamped CO2 conditions (Golestani & Chen, 2020). In the 'clamped' condition, participant's end-tidal CO2 (PETCO2) levels were clamped to their average PETCO2 level using the RespirAct™ breathing circuit (Thornhill Research, Toronto, Canada). For the free-breathing condition, participants were allowed to breathe freely over the course of the scan. Detailed MRI acquisition parameters are provided in Golestani & Chen (2020). Briefly, anatomical T1-weighted structural and single-echo, multiband EPI BOLD-fMRI scans were collected on a Siemens TIM Trio 3T MRI scanner with a 32-channel head coil. Free-breathing and clamped CO2 fMRI recordings were acquired with TR = 380ms, TE = 30ms, multiband acceleration factor = 3, flip angle = 40 degrees and voxel size = 4x4x5 mm3.

Quality Control of Physiological Recordings

Peripheral physiological recordings tend to be noisy, with relative noise levels dependent on their placement location, subject compliance and movement. To ensure our analysis was not affected by acquisition artifacts of the physiological recordings, raw signals from all subjects in each dataset were visually inspected before inclusion. Several qualitative criteria for each signal type were employed to determine physiological signals for inclusion in the analysis. PPG signals were inspected for 1) clearly visible pulsatile waveforms across the entire recording session and 2) the infrequent occurrence of high amplitude noise artifacts. Respiratory belt signals were inspected for 1) clearly visible respiratory time courses reflecting the peak and trough of the abdomen during the respiratory cycle and 2) the absence of prominent ceiling or floor effects/cut-offs at peaks of the respiratory waveform. The primary criteria for the minimally preprocessed pupil diameter time courses were the absence of multiple, long duration (subjectively determined) eye closures or blinks. Skin conductance time courses for the NKI-REST and NKI-TASK dataset were inspected for 1) prominent low-frequency fluctuations visible from background noise, and 2) the absence of extreme, sudden jumps/drops in baseline signal.

MRI Data Preprocessing

Excluding the ME-REST, ME-TASK, ME-TASK-CUE and HCP-REST datasets, datasets were received in raw (unprocessed) NIFTI formats. Depending on the nature of the EPI-BOLD acquisition, the nine datasets were processed with slightly different preprocessing pipelines. We first describe dataset-specific preprocessing, and then describe the common preprocessing steps that were applied to all datasets following dataset-specific preprocessing. All preprocessing steps were performed in either *Nipype* (Gorgolewski et al., 2011) with calls to *FSL* utilities, or *AFNI* (for multi-echo preprocessing).

Dataset Specific Preprocessing

For the ME-REST, ME-TASK and ME-TASK-CUE datasets, more comprehensive preprocessing details are provided in Goodale et al. (2021). Briefly, the EPI-BOLD preprocessing pipeline consisted of the following steps: the first 7 volumes were removed, six-parameter rigid body motion correction and slice timing correction with *3dvolreg* and *3dTshift* in AFNI (https://afni.nimh.nih.gov/), Multi-Echo ICA denoising and optimal combination of echos using Tedana software (DuPre et al., 2020), non-linear registration to the MNI152 template using SPM software (https://www.fil.ion.ucl.ac.uk/spm/), removal of spikes (outliers) from the time courses using 3dDespike in AFNI, and spatial smoothing with a gaussian kernel (FWHM=3mm) in AFNI.

For the HCP-REST dataset, we used EPI-BOLD scans previously preprocessed with the HCP's ICA-based artifact removal process (Smith et al., 2013) to minimize effects of spatially structured noise in our analysis. EPI scans were previously motion-corrected, registered to the MNI152 template, and intensity normalized. Comprehensive details of the HCP preprocessing pipeline are described in Glasser et al. (2013) .

The NKI-REST, NKI-TASK, YALE-REST, NATVIEW-REST and clamped CO2 datasets shared a largely similar set of preprocessing steps. First, the first N volumes (~10s) of the NKI-REST (7), NKI-TASK (7), YALE-REST (10), and clamped CO2 (26) EPI BOLD scans were dropped to remove non-steady state time points. For the NATVIEW-REST dataset, the last 2 volumes were dropped to align with the EEG and pupillometry recordings (no volumes were dropped from the start of the scan). Slice timing correction was applied to the EPI-BOLD scans of the NATVIEW-REST dataset using the *FSL slicetimer* utility due to its longer TR acquisition (TR=2.1s). Second, EPI-BOLD scans from all datasets were motion corrected with six-parameter rigid body alignment with FSL *MCFLIRT.* EPI-BOLD scans were then non-linearly registered to the MNI152 template using FSL's FMRIB's Nonlinear Image Registration Tool (FNIRT) (Andersson et al., 2010).

For the ME-REST-SUPP dataset, EPI-BOLD scans went through the following preprocessing steps: motion and slice time correction using *3dvolreg* and *3dTshift* in AFNI, respectively, Multi-Echo ICA denoising and optimal combination of echos using Tedana software (DuPre et al., 2020), and non-linear registration to the MNI152 template using FSL's FNIRT.

Common Preprocessing

Following dataset-specific preprocessing, all datasets were then resampled to 3mm (isotropic) MNI152 space. Excluding the ME-REST, ME-TASK, ME-TASK-CUE and HCP-REST datasets, this resampling step occurred during FNIRT registration. For the clamped CO2 dataset, fMRI volumes were resampled to 4mm (isotropic) MNI152 space to more closely match its spatial sampling. Following resampling, fMRI volumes were spatially smoothed with a gaussian kernel (FWHM=5mm) using FSL and temporally filtered with a fifth-order Butterworth bandpass zero-phase filter (0.01-0.1Hz). For all datasets, voxels were extracted with a dilated MNI152 brain mask, so as to pick up voxel time courses in large dural venous sinuses and CSF compartments.

EEG Preprocessing

Preprocessing of EEG recordings in the ME-REST, ME-TASK and ME-TASK-CUE datasets are described in (Goodale et al., 2021). Briefly, channel time courses were first corrected for gradient artifacts through the average artifact subtraction method (Allen et al., 2000). Ballistocardiogram artifacts were removed by subtraction of an average artifact template locked to cardiac R-peaks, followed by independent component analysis (ICA) of the template-subtracted time courses. The scalp EEG channel time courses were referenced to channel FCz for analysis.These EEG preprocessing steps were performed with the BrainVision Analyzer software.

Preprocessing of EEG recordings for the NATVIEW-REST dataset was performed with custom EEGLAB MATLAB scripts provided by the authors of the dataset (https://github.com/NathanKlineInstitute/NATVIEW_EEGFMRI) and are described in (Telesford et al., 2023). Briefly, the preprocessing steps included 1) gradient artifact removal with the FASTR utility from the EEGLAB FMRIB Plugin, 2) QRS/heartbeat detection using the ECG

channel, followed by pulse artifact correction with a template subtraction method, and 3) bandpass filtered between 0.3 to 50Hz using a Hamming windowed sinc FIR filter. Scalp EEG time courses were referenced to the common average for analysis.

Physiological and EEG Feature Extraction

Six physiological signals were extracted from the raw PPG, respiration belt, skin conductance, and pupil diameter recordings. Heart rate variability, systolic peak amplitude (PPG pulse amplitude) and low-frequency (0.01-0.1Hz) PPG signals were extracted from raw PPG recordings. Respiratory volume (Harrison et al., 2021) was extracted from the raw respiration belt recordings. Low-frequency (0.01-0.1Hz) tonic skin conductance was extracted from the raw skin conductance signals. We used minimally-preprocessed pupil diameter signals extracted from eye-tracking recordings provided by the authors for the NATVIEW-REST and YALE-REST datasets. For comparison with BOLD fMRI signals, the extracted physiological signals were clipped at five standard deviations from the mean (for outlier removal), resampled to the length of the functional MRI scan and filtered using a fifth-order Butterworth bandpass filter (0.01-0.1Hz) excluding the low-frequency PPG and tonic skin conductance signals that were already filtered. Note: the minimally-preprocessed pupil diameter signals from the YALE-REST dataset were already resampled to the length of the functional scan. Details of the preprocessing for each physiological signal are provided below. The preprocessing pipeline for the physiological signals (and EEG signals) is illustrated in **Supplementary Figure 7.**

Heart rate variability time courses were extracted from PPG time courses using the NeuroKit2 package (https://neuropsychology.github.io/NeuroKit/index.html) in Python. For calculation of HR, the raw PPG time course was first filtered with a third-order Butterworth bandpass filter (0.5 - 8Hz) followed by systolic peak detection using the method by Elgendi et al. (2013). Heart rate was calculated from the period of time between peaks and interpolated to the same length of the raw signal with monotone cubic interpolation (Fritsch & Butland, 1984). For extraction of PPG pulse amplitude signals, the amplitude of the systolic peaks (previously identified by the peak detection method) were interpolated with monotone cubic interpolation.

Work by Tong et al. (2012) found that widespread brain hemodynamics were correlated with low-frequency (0.01 - 0.1Hz) oxygenation signals in the periphery measured by near-infrared spectroscopy (NIRS). We assessed whether a similar peripheral low-frequency oxygenation signal was present in the PPG time courses recorded in our datasets. Inspection of the power spectral density estimates of the PPG time courses revealed a detectable, low-frequency signal in the 0.01 - 0.1 Hz range with varying degrees of amplitude across datasets (**Supplementary Figure 5**). For the comparison of this signal with BOLD time courses, we filtered the PPG time courses with a fifth-order Butterworth bandpass filter (0.01-0.1Hz). Low-frequency PPG signals were attenuated in the HCP-REST and ME-REST-SUPP dataset, though detectable (**Supplementary Figure 5**).

For the NKI-REST and NKI-TASK dataset, skin conductance (SC) signals were collected from the hand. SC time courses consist of a low-frequency tonic and high-frequency phasic component (Lykken & Venables, 1971). The tonic component reflects the slowly-varying component of the skin conductance signal, and has previously been studied in the context of fMRI (Nagai et al., 2004). We extracted a narrowband tonic SC signal matching the frequency content of spontaneous resting-state BOLD signals (0.01-0.1Hz) with a fifth-order Butterworth bandpass filter (0.01-0.1Hz).

For the YALE-REST dataset, we used minimally preprocessed pupillometry signals provided by the authors (https://openneuro.org/datasets/ds003673/versions/2.0.1). The minimal preprocessing pipeline consisted of 4-point spline interpolation of eye blinks, low-pass filtering with a Butterworth filter (< 0.5 Hz), removal of the first 10 seconds of recordings (to match the length of the functional scan), and resampling to the sampling frequency of the functional scan (1 Hz). We also used minimally preprocessed pupillometry signals for the NATVIEW-REST dataset. The minimal preprocessing pipeline consisted of linear interpolation of eye blinks, median filter of 0.2 secs width, and resampling to the frequency of the functional scan (0.47Hz).

Respiratory volume (RV) was calculated from respiration belt time courses using a recently developed Hilbert-based method (Harrison et al., 2021), implemented in NeuroKit2. High-frequency noise was first removed from the respiratory belt time courses with a Butterworth tenth-order low-pass filter (< 0.75Hz). Amplitude and phase components were then extracted from the filtered signal via the Hilbert Transform. Following an iterated linear interpolation procedure of the phase time courses, RV was calculated as the product of the derivative of the interpolated phase time course (i.e. the instantaneous breathing rate) with the signal amplitude (breathing depth/amplitude).

EEG power and vigilance fluctuations were extracted from averaged parietal and occipital lobe EEG channel time courses (ME-REST/TASK: P3, P4, Pz, O1, O2, Oz; NATVIEW-REST: P3,P4, P7, P8, Pz, POz, P1, P2, PO3, PO4, P5, P6, PO7, PO8, O1, O2, Oz) using the MNE-Python package (Gramfort et al., 2013) (https://mne.tools/stable/index.html). Time-frequency EEG power was extracted via Morlet wavelet filters (number of cycles = 15) to construct a filter bank ranging from 2 to 20Hz (spanning Delta, Theta and Alpha oscillation bands). For the ME-REST and NATVIEW-REST dataset, power was extracted from each signal in the filter bank and was cross-correlated with time courses from the first principal component of the fMRI data (see below). Alpha power signals were computed through band-pass FIR filtering (Hamming window; 8 - 12Hz) of the average channel time course, followed by extraction of instantaneous amplitude via the Hilbert Transform. For comparison with fMRI time courses in the ME-REST and NATVIEW-REST dataset, EEG power time courses were resampled to the length of the fMRI scan.

K-Complex Annotation

Event-related averaging of fMRI and physiological signals around K-complex onsets was performed on a subset (N=7) of participants from the ME-REST dataset who fell asleep during

their scanning session. K-complex annotations were performed in a semi-automated fashion. First, EEG time courses from frontal and central channels were automatically sleep staged using the yasa package in Python (https://github.com/raphaelvallat/yasa; Vallat & Walker, 2021) with default parameters. Following automated sleep-staging, EEG time courses from sleep stage II were manually annotated for K-complex onsets according to AASM criteria (Berry et al., 2017) using a custom bipolar montage. Separate K-complexes that occurred within a window of ~30s were removed before event-related averaging to avoid overlapping responses.

Principal Component Analysis

As in Bolt et al. (2022), the zero-lag and time-lag structure of the global BOLD signal was modeled with principal component analysis (PCA) and complex principal component analysis (CPCA), respectively. As shown in Bolt et al. (2022), the first principal component of both PCA and CPCA extract a pattern of global BOLD fluctuations that is closely correlated (in time) with the global mean time course. Standard PCA was used to extract the simultaneous statistical dependence between cortical areas of global BOLD fluctuations, CPCA was used to extract time-lag statistical dependence (i.e. traveling wave or propagatory behavior). In this study, we analyze the properties of the first principal component in volume space, including signals from subcortical structures, ventricles and cerebral sinuses.

CPCA involves the application of PCA to complex-valued time courses generated by the Hilbert transform. We extracted the first complex principal component using CPCA on the complex-valued (bandpassed to 0.01-0.1Hz) BOLD time courses temporally-concatenated across subjects. Time-lag information can be extracted from the phase representation of the complex-valued PC (via Euler's Identity). The phase representation encodes the time-delay between voxels (in radians) within the first complex PC. The time-lag information can also be visualized over selected time points via a temporal reconstruction (**Supplementary Movie 1**). Comprehensive details are provided in Bolt et al. (2022). Briefly, we first divided the temporal phase time courses of the first complex PC into equally-spaced bins (N=30). We then projected the complex PC back into voxel space to derive voxel time courses. Finally, we averaged the real-valued voxel time courses within the time points indexed by the equally-spaced phase bins. This resulted in a 30-volume 'movie' that visualizes the temporal evolution of a component. Both PCA and CPCA solutions were computed using a fast randomized SVD algorithm developed by *Facebook* (https://github.com/facebookarchive/fbpca). More details of the CPCA algorithm can be found in Bolt et al. (2022).

Cross-Correlation Analyses

For the ME-REST, HCP-REST, ME-REST-SUPP, NKI-REST and YALE-REST datasets, cross-correlation analyses were conducted between the electrophysiological time courses and the first principal component (PC1) time course. Product-moment cross-correlations were computed at the subject-level and group-average cross-correlations were computed by the mean of the subject-level cross-correlations. For comparability across datasets with different

sampling rates, we interpolated subject and group-average cross-correlation functions with a cubic spline from -30s to 30s (time-lag).

Impulse Response Modeling of Physiological Signals

To summarize the temporal dynamics of all recorded physiological signals in response to fluctuations in global BOLD signals (i.e. PC1), we implemented a linear systems modeling approach as described in Chang et al. (2009). Impulse response functions were estimated separately for each physiological signal through deconvolution of the physiological signal using a Gaussian Process prior. A Gaussian Process prior is used to capture the underlying smoothness of the physiological signal. The deconvolved physiological signal is estimated from the maximum *a posteriori* (MAP) of the posterior distribution. As no single dataset contained all physiological signals, we superimposed the deconvolved physiological impulse responses from three separate datasets: ME-REST (PPG signals, Alpha EEG power, and respiratory volume), NATVIEW-REST (pupil), and NKI-REST datasets (skin conductance). The length scale and kernel variance hyperparameters of the Gaussian Process, were set to 3 and 1, respectively. Negative shifts of the signal were included to ensure that physiological responses before the peak of the global BOLD signal were captured.

Multi-Set Canonical Correlation Analysis

To estimate the *joint* fluctuations between physiological and the first principal component time courses, we implemented a multi-set canonical correlation analysis (MCCA) on the full set of signals in each dataset (Kettenring, 1971). Each 'set' was formed from time lags of a single physiological signal. Inclusion of all potential time lags out to a window size N leads to potential collinearity and risks overfitting. Instead, we implement a generalized additive distributed lag approach (Gasparrini et al., 2010; Zanobetti et al., 2000), where time-lagged predictors for each physiological signal were generated via a linear combination of time-lagged copies of the signal with a natural cubic spline basis with three splines distributed across the time window (from 0 to 10s; number of time points varied for each dataset due to different sampling rates). The resulting time-lagged predictor is represented by three linear-weighted versions of the original signal encoding a smooth curve across the time window.

The objective of MCCA is to find a linear-weighted combination of the time-lagged copies of each signal that maximizes the pairwise correlations between all signals. MCCA was performed at the group-level by group-wise temporal concatenation. The number of 'sets' in the MCCA analysis varied across datasets due to the differing number of physiological signals recorded across datasets. We extract the first canonical component from the MCCA algorithm, corresponding to the linear weighted combination of all signals that produces the maximum pairwise correlation between signals. The MCCA algorithm was implemented in the cca-zoo

Python package (https://github.com/jameschapman19/cca_zoo). Illustration of the MCCA approach used in our study is provided in **Supplementary Figure 8**.

Statistical significance testing of the average pairwise correlation of the first canonical component was performed using block-wise permutation of subject time courses before temporal concatenation across subjects. Specifically, physiological signals were randomly shuffled across subjects before temporal concatenation, effectively removing cross-signal couplings while preserving the autocorrelation structure within each signal. For example, one permutation may align signal A in subject 1, with signal B in subject 7, and so forth. For each permutation (N=1000), the average pairwise correlation between all permuted time courses of the first canonical component was extracted to construct a null distribution.

Event-Related Averages

Event-related averaging of the ME-TASK, NKI-TASK and ME-REST datasets was performed to examine the hemodynamic and physiological response to deep breaths, breath holds and spontaneous K-complex onsets, respectively. A group-level response function for each physiological signal was generated by averaging across all trials and subjects within a window starting from onset out to ~29s. Standard error plots for each group-level response function were generated via cluster bootstrapping, where trials within each subject were randomly resampled with replacement (N = 100) before averaging.

For the ME-TASK dataset, event-related EEG power fluctuations were examined for each subject by averaging Wavelet filter bank power signals (i.e. time-frequency spectral power in 2-20Hz frequencies; see above) within a 20s window post breath-onset across trials. Baseline log-ratio normalization (i.e. decibels) was applied to the subject-averaged time courses with the time span 1s before up until stimulus onset as the baseline. A group event-related average was constructed from averaging across event-related subject averages.

For the ME-TASK-CUE dataset, event-related averaging of physiological and EEG power time courses was conducted using the same procedure as the ME-TASK dataset. Some inter-trial intervals between auditory cues were shorter for this task, on average (range: ~8 to 89 secs), relative to to the ME-TASK dataset. Trials separated by less than 30s were excluded. In addition, trials with a non-response (i.e. no button response) were excluded.

References

Allen, P. J., Josephs, O., & Turner, R. (2000). A Method for Removing Imaging Artifact from Continuous EEG Recorded during Functional MRI. *NeuroImage*, *12*(2), 230–239.

https://doi.org/10.1006/nimg.2000.0599

Anaclet, C., & Fuller, P. M. (2017). Brainstem regulation of slow-wave-sleep. *Current Opinion in Neurobiology*, *44*, 139–143. https://doi.org/10.1016/j.conb.2017.04.004

Andersson, J., Jenkinson, M., & Smith, S. (2010). Non-linear registration, aka spatial normalization. *FMRIB Technical Report TR07JA2*.

Ashhad, S., Kam, K., Del Negro, C. A., & Feldman, J. L. (2022). Breathing Rhythm and Pattern and Their Influence on Emotion. *Annual Review of Neuroscience*, *45*(1), 223–247. https://doi.org/10.1146/annurev-neuro-090121-014424

Battisti-Charbonney, A., Fisher, J., & Duffin, J. (2011). The cerebrovascular response to carbon dioxide in humans. *The Journal of Physiology*, *589*(Pt 12), 3039. https://doi.org/10.1113/jphysiol.2011.206052

Berry, R. B., Brooks, R., Gamaldo, C., Harding, S. M., Lloyd, R. M., Quan, S. F., Troester, M. T., & Vaughn, B. V. (2017). AASM Scoring Manual Updates for 2017 (Version 2.4). *Journal of Clinical Sleep Medicine : JCSM : Official Publication of the American Academy of Sleep Medicine*, *13*(5), 665–666. https://doi.org/10.5664/jcsm.6576

Birn, R. M., Diamond, J. B., Smith, M. A., & Bandettini, P. A. (2006). Separating respiratory-variation-related fluctuations from neuronal-activity-related fluctuations in fMRI. *NeuroImage*, *31*(4), 1536–1548. https://doi.org/10.1016/j.neuroimage.2006.02.048

Birn, R. M., Smith, M. A., Jones, T. B., & Bandettini, P. A. (2008). The Respiration Response Function: The temporal dynamics of fMRI signal fluctuations related to changes in respiration. *NeuroImage*, *40*(2), 644–654. https://doi.org/10.1016/j.neuroimage.2007.11.059

Bolt, T., Nomi, J. S., Bzdok, D., Salas, J. A., Chang, C., Thomas Yeo, B. T., Uddin, L. Q., & Keilholz, S. D. (2022). A parsimonious description of global functional brain organization in three spatiotemporal patterns. *Nature Neuroscience*, *25*(8), Article 8. https://doi.org/10.1038/s41593-022-01118-1

Buxton, R. B., Uludağ, K., Dubowitz, D. J., & Liu, T. T. (2004). Modeling the hemodynamic response to brain activation. *NeuroImage*, *23*, S220–S233. https://doi.org/10.1016/j.neuroimage.2004.07.013

Cash, S. S., Halgren, E., Dehghani, N., Rossetti, A. O., Thesen, T., Wang, C., Devinsky, O., Kuzniecky, R., Doyle, W., Madsen, J. R., Bromfield, E., Erőss, L., Halász, P., Karmos, G., Csercsa, R., Wittner, L., & Ulbert, I. (2009). The Human K-Complex Represents an Isolated Cortical Down-State. *Science (New York, N.Y.)*, *324*(5930), 1084–1087. https://doi.org/10.1126/science.1169626

Chang, C., Cunningham, J. P., & Glover, G. H. (2009). Influence of heart rate on the BOLD signal: The cardiac response function. *NeuroImage*, *44*(3), 857–869. https://doi.org/10.1016/j.neuroimage.2008.09.029

Claassen, J. A. H. R., Thijssen, D. H. J., Panerai, R. B., & Faraci, F. M. (2021). Regulation of cerebral blood flow in humans: Physiology and clinical implications of autoregulation. *Physiological Reviews*, *101*(4), 1487–1559. https://doi.org/10.1152/physrev.00022.2020

Dringenberg, H. C., & Vanderwolf, C. H. (1998). Involvement of Direct and Indirect Pathways in Electrocorticographic Activation. *Neuroscience & Biobehavioral Reviews*, *22*(2), 243–257. https://doi.org/10.1016/S0149-7634(97)00012-2

DuPre, E., Salo, T., Markello, R., Kundu, P., Whitaker, K., & Handwerker, D. (2020). *ME-ICA/tedana: 0.0.9a* [Computer software]. Zenodo. https://doi.org/10.5281/zenodo.3786890

Elgendi, M., Norton, I., Brearley, M., Abbott, D., & Schuurmans, D. (2013). Systolic peak detection in acceleration photoplethysmograms measured from emergency responders in tropical conditions. *PloS One*, *8*(10), e76585. https://doi.org/10.1371/journal.pone.0076585

Falahpour, M., Chang, C., Wong, C. W., & Liu, T. T. (2018). Template-based prediction of vigilance fluctuations in resting-state fMRI. *NeuroImage*, *174*, 317–327.

https://doi.org/10.1016/j.neuroimage.2018.03.012

Fox, M. D., & Raichle, M. E. (2007). Spontaneous fluctuations in brain activity observed with functional magnetic resonance imaging. *Nature Reviews Neuroscience*, *8*(9), Article 9. https://doi.org/10.1038/nrn2201

Fritsch, F. N., & Butland, J. (1984). A Method for Constructing Local Monotone Piecewise Cubic Interpolants. *SIAM Journal on Scientific and Statistical Computing*, *5*(2), 300–304. https://doi.org/10.1137/0905021

Gasparrini, A., Armstrong, B., & Kenward, M. G. (2010). Distributed lag non-linear models. *Statistics in Medicine*, *29*(21), 2224–2234. https://doi.org/10.1002/sim.3940

Glasser, M. F., Sotiropoulos, S. N., Wilson, J. A., Coalson, T. S., Fischl, B., Andersson, J. L., Xu, J., Jbabdi, S., Webster, M., Polimeni, J. R., Van Essen, D. C., Jenkinson, M., & WU-Minn HCP Consortium. (2013). The minimal preprocessing pipelines for the Human Connectome Project. *NeuroImage*, *80*, 105–124. https://doi.org/10.1016/j.neuroimage.2013.04.127

Golestani, A. M., & Chen, J. J. (2020). Controlling for the effect of arterial-CO2 fluctuations in resting-state fMRI: Comparing end-tidal CO2 clamping and retroactive CO2 correction. *NeuroImage*, *216*, 116874. https://doi.org/10.1016/j.neuroimage.2020.116874

Goodale, S. E., Ahmed, N., Zhao, C., de Zwart, J. A., Özbay, P. S., Picchioni, D., Duyn, J., Englot, D. J., Morgan, V. L., & Chang, C. (2021). fMRI-based detection of alertness predicts behavioral response variability. *eLife*, *10*, e62376. https://doi.org/10.7554/eLife.62376

Gorgolewski, K., Burns, C. D., Madison, C., Clark, D., Halchenko, Y. O., Waskom, M. L., & Ghosh, S. S. (2011). Nipype: A flexible, lightweight and extensible neuroimaging data processing framework in python. *Frontiers in Neuroinformatics*, *5*, 13. https://doi.org/10.3389/fninf.2011.00013

Gramfort, A., Luessi, M., Larson, E., Engemann, D., Strohmeier, D., Brodbeck, C., Goj, R., Jas,

M., Brooks, T., Parkkonen, L., & Hämäläinen, M. (2013). MEG and EEG data analysis with MNE-Python. *Frontiers in Neuroscience*, *7*. https://www.frontiersin.org/articles/10.3389/fnins.2013.00267

Gu, Y., Han, F., Sainburg, L. E., Schade, M. M., Buxton, O. M., Duyn, J. H., & Liu, X. (2022). An orderly sequence of autonomic and neural events at transient arousal changes. *NeuroImage*, *264*, 119720. https://doi.org/10.1016/j.neuroimage.2022.119720

Halász, P., Terzano, M., Parrino, L., & Bódizs, R. (2004). The nature of arousal in sleep. *Journal of Sleep Research*, *13*(1), 1–23. https://doi.org/10.1111/j.1365-2869.2004.00388.x

Hamner, J. w., Tan, C. O., Lee, K., Cohen, M. A., & Taylor, J. A. (2010). Sympathetic Control of the Cerebral Vasculature in Humans. *Stroke*, *41*(1), 102–109. https://doi.org/10.1161/STROKEAHA.109.557132

Harrison, S. J., Bianchi, S., Heinzle, J., Stephan, K. E., Iglesias, S., & Kasper, L. (2021). A Hilbert-based method for processing respiratory timeseries. *NeuroImage*, *230*, 117787. https://doi.org/10.1016/j.neuroimage.2021.117787

Ito, J., Roy, S., Liu, Y., Cao, Y., Fletcher, M., Lu, L., Boughter, J. D., Grün, S., & Heck, D. H. (2014). Whisker barrel cortex delta oscillations and gamma power in the awake mouse are linked to respiration. *Nature Communications*, *5*(1), 3572. https://doi.org/10.1038/ncomms4572

Kettenring, J. R. (1971). Canonical Analysis of Several Sets of Variables. *Biometrika*, *58*(3), 433–451. https://doi.org/10.2307/2334380

Khoo, M. C. K., & Chalacheva, P. (2019). Respiratory modulation of peripheral vasoconstriction: A modeling perspective. *Journal of Applied Physiology*, *127*(5), 1177–1186. https://doi.org/10.1152/japplphysiol.00111.2019

Kish, B., Chen, J. J., & Tong, Y. (2023). Effects of clamping end-tidal CO2 on neurofluidic low-frequency oscillations. *NMR in Biomedicine*, e5084. https://doi.org/10.1002/nbm.5084

Kluger, D. S., & Gross, J. (2021). Respiration modulates oscillatory neural network activity at rest. *PLOS Biology*, *19*(11), e3001457. https://doi.org/10.1371/journal.pbio.3001457

Koep, J. L., Taylor, C. E., Coombes, J. S., Bond, B., Ainslie, P. N., & Bailey, T. G. (2022). Autonomic control of cerebral blood flow: Fundamental comparisons between peripheral and cerebrovascular circulations in humans. *The Journal of Physiology*, *600*(1), 15–39. https://doi.org/10.1113/JP281058

Lee, K., Horien, C., O'Connor, D., Garand-Sheridan, B., Tokoglu, F., Scheinost, D., Lake, E. M. R., & Constable, R. T. (2022). Arousal impacts distributed hubs modulating the integration of brain functional connectivity. *NeuroImage*, *258*, 119364. https://doi.org/10.1016/j.neuroimage.2022.119364

Liu, T. T., Nalci, A., & Falahpour, M. (2017). The Global Signal in fMRI: Nuisance or Information? *NeuroImage*, *150*, 213–229. https://doi.org/10.1016/j.neuroimage.2017.02.036

Lykken, D. T., & Venables, P. H. (1971). Direct Measurement of Skin Conductance: A Proposal for Standardization. *Psychophysiology*, *8*(5), 656–672. https://doi.org/10.1111/j.1469-8986.1971.tb00501.x

Lynch, C. J., Silver, B. M., Dubin, M. J., Martin, A., Voss, H. U., Jones, R. M., & Power, J. D. (2020). Prevalent and sex-biased breathing patterns modify functional connectivity MRI in young adults. *Nature Communications*, *11*(1), Article 1. https://doi.org/10.1038/s41467-020-18974-9

Markiewicz, C. J., Gorgolewski, K. J., Feingold, F., Blair, R., Halchenko, Y. O., Miller, E., Hardcastle, N., Wexler, J., Esteban, O., Goncavles, M., Jwa, A., & Poldrack, R. (2021). The OpenNeuro resource for sharing of neuroscience data. *eLife*, *10*, e71774. https://doi.org/10.7554/eLife.71774

Marumo, C., & Nakano, T. (2021). Early phase of pupil dilation is mediated by the peripheral parasympathetic pathway. *Journal of Neurophysiology*, *126*(6), 2130–2137. https://doi.org/10.1152/jn.00401.2021

Murphy, K., & Fox, M. D. (2017). Towards a consensus regarding global signal regression for resting state functional connectivity MRI. *NeuroImage*, *154*, 169–173. https://doi.org/10.1016/j.neuroimage.2016.11.052

Nagai, Y., Critchley, H. D., Featherstone, E., Trimble, M. R., & Dolan, R. J. (2004). Activity in ventromedial prefrontal cortex covaries with sympathetic skin conductance level: A physiological account of a “default mode” of brain function. *NeuroImage*, *22*(1), 243–251. https://doi.org/10.1016/j.neuroimage.2004.01.019

Nooner, K., Colcombe, S., Tobe, R., Mennes, M., Benedict, M., Moreno, A., Panek, L., Brown, S., Zavitz, S., Li, Q., Sikka, S., Gutman, D., Bangaru, S., Schlachter, R. T., Kamiel, S., Anwar, A., Hinz, C., Kaplan, M., Rachlin, A., … Milham, M. (2012). The NKI-Rockland Sample: A Model for Accelerating the Pace of Discovery Science in Psychiatry. *Frontiers in Neuroscience*, *6*. https://www.frontiersin.org/articles/10.3389/fnins.2012.00152

Özbay, P. S., Chang, C., Picchioni, D., Mandelkow, H., Chappel-Farley, M. G., van Gelderen, P., de Zwart, J. A., & Duyn, J. (2019). Sympathetic activity contributes to the fMRI signal. *Communications Biology*, *2*(1), 1–9. https://doi.org/10.1038/s42003-019-0659-0

Power, J. D., Lynch, C. J., Silver, B. M., Dubin, M. J., Martin, A., & Jones, R. M. (2019). Distinctions among real and apparent respiratory motions in human fMRI data. *NeuroImage*, *201*, 116041. https://doi.org/10.1016/j.neuroimage.2019.116041

Power, J. D., Plitt, M., Laumann, T. O., & Martin, A. (2017). Sources and implications of whole-brain fMRI signals in humans. *NeuroImage*, *146*, 609–625. https://doi.org/10.1016/j.neuroimage.2016.09.038

Raut, R. V., Rosenthal, Z. P., Wang, X., Miao, H., Zhang, Z., Lee, J.-M., Raichle, M. E., Bauer, A. Q., Brunton, S. L., Brunton, B. W., & Kutz, J. N. (2023). *Arousal as a universal embedding for spatiotemporal brain dynamics* (p. 2023.11.06.565918). bioRxiv. https://doi.org/10.1101/2023.11.06.565918

Raut, R. V., Snyder, A. Z., Mitra, A., Yellin, D., Fujii, N., Malach, R., & Raichle, M. E. (2021).

Global waves synchronize the brain's functional systems with fluctuating arousal. *Science Advances*, *7*(30), eabf2709. https://doi.org/10.1126/sciadv.abf2709

Samuels, E. R., & Szabadi, E. (2008). Functional Neuroanatomy of the Noradrenergic Locus Coeruleus: Its Roles in the Regulation of Arousal and Autonomic Function Part II: Physiological and Pharmacological Manipulations and Pathological Alterations of Locus Coeruleus Activity in Humans. *Current Neuropharmacology*, *6*(3), 254–285. https://doi.org/10.2174/157015908785777193

Satpute, A. B., Kragel, P. A., Barrett, L. F., Wager, T. D., & Bianciardi, M. (2019). Deconstructing arousal into wakeful, autonomic and affective varieties. *Neuroscience Letters*, *693*, 19–28. https://doi.org/10.1016/j.neulet.2018.01.042

Shams, S., LeVan, P., & Chen, J. J. (2021). The neuronal associations of respiratory-volume variability in the resting state. *NeuroImage*, *230*, 117783. https://doi.org/10.1016/j.neuroimage.2021.117783

Smith, S. M., Andersson, J., Auerbach, E. J., Beckmann, C. F., Bijsterbosch, J., Douaud, G., Duff, E., Feinberg, D. A., Griffanti, L., Harms, M. P., Kelly, M., Laumann, T., Miller, K. L., Moeller, S., Petersen, S., Power, J., Salimi-Khorshidi, G., Snyder, A. Z., Vu, A., … Glasser, M. F. (2013). Resting-state fMRI in the Human Connectome Project. *NeuroImage*, *80*, 144–168. https://doi.org/10.1016/j.neuroimage.2013.05.039

Spreng, R. N., Setton, R., Alter, U., Cassidy, B. N., Darboh, B., DuPre, E., Kantarovich, K., Lockrow, A. W., Mwilambwe-Tshilobo, L., Luh, W.-M., Kundu, P., & Turner, G. R. (2022). Neurocognitive aging data release with behavioral, structural and multi-echo functional MRI measures. *Scientific Data*, *9*(1), Article 1. https://doi.org/10.1038/s41597-022-01231-7

Telesford, Q. K., Gonzalez-Moreira, E., Xu, T., Tian, Y., Colcombe, S., Cloud, J., Russ, B. E., Falchier, A., Nentwich, M., Madsen, J., Parra, L., Schroeder, C., Milham, M., & Franco, A. R. (2023). *An open-access dataset of naturalistic viewing using simultaneous*

EEG-fMRI (p. 2022.11.23.517540). bioRxiv. https://doi.org/10.1101/2022.11.23.517540

Tong, Y., Hocke, L. M., Licata, S. C., & deB. Frederick, B. (2012). Low-frequency oscillations measured in the periphery with near-infrared spectroscopy are strongly correlated with blood oxygen level-dependent functional magnetic resonance imaging signals. *Journal of Biomedical Optics*, *17*(10), 106004. https://doi.org/10.1117/1.JBO.17.10.106004

Vallat, R., & Walker, M. P. (2021). An open-source, high-performance tool for automated sleep staging. *eLife*, *10*, e70092. https://doi.org/10.7554/eLife.70092

Van Essen, D. C., Smith, S. M., Barch, D. M., Behrens, T. E. J., Yacoub, E., Ugurbil, K., & WU-Minn HCP Consortium. (2013). The WU-Minn Human Connectome Project: An overview. *NeuroImage*, *80*, 62–79. https://doi.org/10.1016/j.neuroimage.2013.05.041

van Lieshout, J. J., & Secher, N. H. (2008). Point:Counterpoint: Sympathetic activity does/does not influence cerebral blood flow. *Journal of Applied Physiology*, *105*(4), 1364–1366. https://doi.org/10.1152/japplphysiol.90597.2008

Wise, R. G., Ide, K., Poulin, M. J., & Tracey, I. (2004). Resting fluctuations in arterial carbon dioxide induce significant low frequency variations in BOLD signal. *NeuroImage*, *21*(4), 1652–1664. https://doi.org/10.1016/j.neuroimage.2003.11.025

Wong, C. W., Olafsson, V., Tal, O., & Liu, T. T. (2013). The amplitude of the resting-state fMRI global signal is related to EEG vigilance measures. *NeuroImage*, *83*, 983–990. https://doi.org/10.1016/j.neuroimage.2013.07.057

Wu, P., Bandettini, P. A., Harper, R. M., & Handwerker, D. A. (2015). Effects of Thoracic Pressure Changes on MRI Signals in the Brain. *Journal of Cerebral Blood Flow & Metabolism*, *35*(6), 1024–1032. https://doi.org/10.1038/jcbfm.2015.20

Yackle, K., Schwarz, L. A., Kam, K., Sorokin, J. M., Huguenard, J. R., Feldman, J. L., Luo, L., & Krasnow, M. A. (2017). Breathing control center neurons that promote arousal in mice. *Science*, *355*(6332), 1411–1415. https://doi.org/10.1126/science.aai7984

Yasuma, F., & Hayano, J.-I. (2004). Respiratory sinus arrhythmia: Why does the heartbeat

synchronize with respiratory rhythm? *Chest*, *125*(2), 683–690. https://doi.org/10.1378/chest.125.2.683

Yellin, D., Berkovich-Ohana, A., & Malach, R. (2015). Coupling between pupil fluctuations and resting-state fMRI uncovers a slow build-up of antagonistic responses in the human cortex. *NeuroImage*, *106*, 414–427. https://doi.org/10.1016/j.neuroimage.2014.11.034

Yuan, H., Zotev, V., Phillips, R., & Bodurka, J. (2013). Correlated slow fluctuations in respiration, EEG, and BOLD fMRI. *NeuroImage*, *79*, 81–93. https://doi.org/10.1016/j.neuroimage.2013.04.068

Zaccaro, A., Piarulli, A., Laurino, M., Garbella, E., Menicucci, D., Neri, B., & Gemignani, A. (2018). How Breath-Control Can Change Your Life: A Systematic Review on Psycho-Physiological Correlates of Slow Breathing. *Frontiers in Human Neuroscience*, *12*. https://www.frontiersin.org/articles/10.3389/fnhum.2018.00353

Zanobetti, A., Wand, M. P., Schwartz, J., & Ryan, L. M. (2000). Generalized additive distributed lag models: Quantifying mortality displacement. *Biostatistics (Oxford, England)*, *1*(3), 279–292. https://doi.org/10.1093/biostatistics/1.3.279

Zelano, C., Jiang, H., Zhou, G., Arora, N., Schuele, S., Rosenow, J., & Gottfried, J. A. (2016). Nasal Respiration Entrains Human Limbic Oscillations and Modulates Cognitive Function. *Journal of Neuroscience*, *36*(49), 12448–12467. https://doi.org/10.1523/JNEUROSCI.2586-16.2016

Zhang, Q., Roche, M., Gheres, K. W., Chaigneau, E., Kedarasetti, R. T., Haselden, W. D., Charpak, S., & Drew, P. J. (2019). Cerebral oxygenation during locomotion is modulated by respiration. *Nature Communications*, *10*(1), Article 1. https://doi.org/10.1038/s41467-019-13523-5